University of Oslo

Master of Science in Physics

Investigation of the properties in the quasi-continuum of ^{107,108}Pd

by

Tomas Kvalheim Eriksen

SAFE
Department of Physics
Faculty of Mathematics and Natural Sciences

June 1, 2012

Acknowledgements

First of all, I must admit that this work has been time consuming and hard, but also interesting and fun. I am therefore happy to finally be done, but at the same time I would gladly have performed the entire investigation all over again. My interest for nuclear physics has really grown during this work, both because I have learned a lot, and because I have realized that there is still very much to be investigated and explained.

I could not have performed this work all on my own, and I am very grateful for any help I have recieved. First, I would like to thank my main supervisor Magne Guttormsen for the guidance and help he has given me throughout this work. Also, Ann-Cecilie Larsen and Sunniva Siem have provided nescessary counceling which I am grateful for. Further, I am also thankful towards all the other participants of the low energy nuclear physics group at SAFE, for providing a socially nice and academically professional environment, and also for their help in taking shifts at the cyclotron during the experiment. Without them, there would not have been any data to investigate. While mentioning the experiment, I would also like to thank the engineers at OCL for the excellent experimental conditions.

At last, but most important, I would like to use this opportunity to thank my family and my parents for supporting and helping me get where I am today.

Tomas Kvalheim Eriksen,
Oslo, June 1, 2012.

Contents

List of Figures

List of Tables

Chapter 1

Introduction

Atomic nuclei are described to consist of protons and neutrons, which are commonly referred to as nucleons. The nucleons are again described to be composed of quarks and gluons, but this is not relevant because of the relatively low energy range investigated in this work, and the nucleons are here considered to be single particles of their own.

The nucleons are fermions, thus obeying the Pauli exclusion principle, which states that only one fermion of the same kind can occupy the same quantum state at the same time. This leads to specifically allowed, discrete quantum states for a number of fermions enclosed by the same potential. The allowed quantum states in such a confined system are determined by the possible configurations of spin and angular momentum of the constituent fermions, which thus define the energies of the quantum states. A nucleus, being composed by protons and neutrons, is exactly such a confined system of fermions. However, note that the protons and neutrons are different kinds of fermions, and that the total system of the nucleus can then be described by two independent systems, i.e. one for protons and one for neutrons. Fortunately, this fact simplifies models quite a bit.

When all the nucleons of a nucleus are configured in such a way that they occupy the lowest available quantum states, the nucleus is said to be in its ground-state. All other configurations correspond to higher energies, and are referred to as excited states of the nucleus. As nature always seeks the configuration of lowest energy, the nucleus will tend towards its respective ground state after excitation to an excited state has occurred. This is of course if no other, more energetically favorable process is probable, e.g. fission. In order for a nucleon to make the transition from a quantum state of higher, to one of lower energy, the excess energy due to the energy difference has to be dissipated somehow. This is acheived by the process of γ-decay, where the excess energy is dissipated by emitting a γ-ray of energy equal to the energy difference of the states. This process is governed by angular momentum and parity selection rules, and not all transitions are allowed.

Information about the properties of the nucleus, i.e. the confined system of fermions, is obtained by investigation of the excited states and the corresponding γ-ray emissions. At high excitation energies, the number of allowed quantum states is so high that their widths, i.e. the uncertainty in energy of a respective state, overlaps. This region is called the quasi-continuum of excited states, since they cannot be distinguished yet they are essentially discrete. In the quasi-continuum region, the γ-decay from an initial excitation energy E_i to a final excitation energy E_f, can be described by the density of accessible states at the final excitation energy, and the relative probability of emission of a γ-ray of energy $E_\gamma = E_i - E_f$. These properties are called the *level density* and the *γ-ray transmission coefficient* respectively, and the *γ-ray strength function* can be extracted from the γ-ray transmission coefficients by division of a simple energy dependence. These characteristics are used for describing the properties in the quasi-continuum, and will be explained more closely in the main text of this work. A method for extracting them from the experimental data will also be described.

Level densities and γ-ray strength functions are used for calculations of cross sections and neutron capture rates, which are important input parameters in e.g. reactor physics and astrophysical models describing the formation of elements in nucleosynthesis. Small variations in the level densities and the γ-ray strength functions may have significant impact on the calculations, and investigation of these properties are therefore of great interest.

The present work concerns the investigation of properties in the quasi-continuum of the nuclei ^{107,108}Pd. Ultimately, the level densities and γ-ray strength functions will be extracted from experimental data obtained for the nuclei, and be used in the analyses of the quasi-continuum. Most attention will be devoted to the γ-ray strength functions, which are also to be compared to models.

1.1 Motivation

In previous analyses of ^{56,57}Fe [1, 2] and $^{93-98}$Mo [3] isotopes, there is found to be an enhancement in the γ-ray strength function at lower energies, and this character will from now on be referred to as the *upbend*. For ^{95}Mo the upbend has recently been confirmed by a different experimental approach [4]. In similar analyses of $^{116-119}$Sn [5] and ^{121,122}Sn [6], there is no evident signs of an upbend, but a resonance at somewhat higher energies is discovered. This is referred to as the *pygmy resonance*. The pygmy resonance is explained to be due to skin oscillations, where a skin of excess neutrons vibrates with respect to the rest of the nucleus.

The ^{107,108}Pd isotopes to be investigated in this work are situated in the mass region between molybdenum and tin, and the main motivation behind the analysis

is the search for a possible transition between the two characteristics. However, the extraction of level densities and γ-ray strength functions is in addition a good motivation by itself.

Chapter 2

Experimental proceedings

The experiment was performed at the Oslo Cyclotron Laboratory (OCL) at the University of Oslo. The main instrument at OCL is a MC-35 Scanditronix cyclotron, which was used to accelerate ^{3}He ions to an energy of 38 MeV. The accelerated ion-beam was extracted for bombardment of a ^{108}Pd target foil with a thickness of 1 mg/cm^2 and a purity of $\sim$ 98.2%. Bombardment of an equally thick ^{12}C target foil was also performed in order to facilitate calibration of the detectors. The experiment was performed in order to investigate the properties of the nuclei ^{107,108}Pd, which were populated by use of the reactions (^{3}He, α) and (^{3}He, ^{3}He') respectively. The energy of the ejectiles α and ^{3}He, and coincident γ-emissions were measured, and this information combined provides a picture of the exited states of the nuclei and their decay patterns. The detected events were recorded and stored on a computer for later offline sorting and treatment, and the experiment was performed for a period of seven days.

2.1 Experimental setup

2.1.1 Oslo Cyclotron Laboratory

The experimental layout of OCL consists mainly of the MC-35 Scanditronix cyclotron, the various target stations and the beam lines connecting them. A sketch of the infrastructure is shown in Fig. 2.1, where the cyclotron is situated in the lower right corner. The figure also includes a table of the different beam types with corresponding energy ranges and intensities, which are available at the cyclotron. The entire system depicted in Fig. 2.1 has to be under vacuum during an experiment in order to prevent energy loss in collission with air molecules. Therefore, the cyclotron and the target stations are connected with airthight pipes, defining the so called beam line, in which the ion beam is transported. The beam trans-

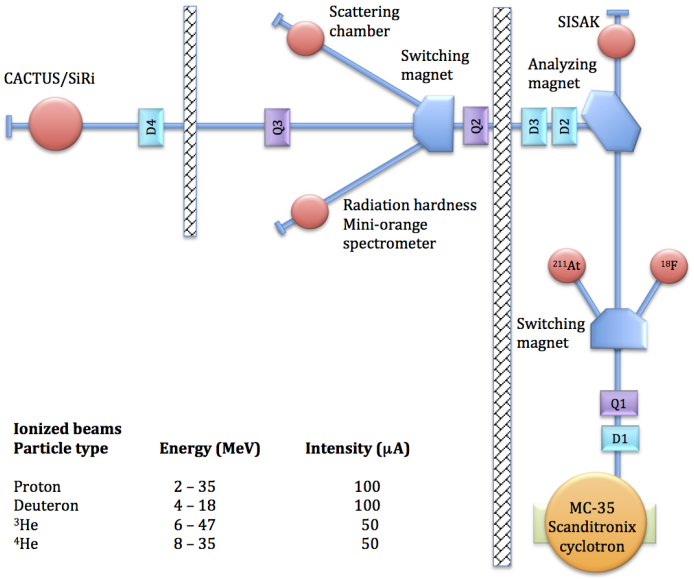

Figure 2.1: The main infrastructure of the experimental setup at the OCL. This figure is taken from the OCL homepage [8].

port, is performed by using adjustable electromagnets and taking advantage of the Lorentz force acting on a charged particle with charge q and velocity $\vec{v}$, moving in a magnetic field $\vec{B}$. The Lorentz force is described by

$$\vec{F} = q \cdot \vec{v} \times \vec{B} \ . \tag{2.1}$$

As seen in Fig. 2.1, there are various magnet arrangements along the beam line. The dipole magnets "D" and quadrupole magnets "Q" direct and focus the beam respectively, the "Switching magnets" are used to select desired beamline, and the "Analyzing magnet" bends the beam 90° towards the target station labeled "CACTUS/SiRi". A great advantage of the analyzing magnet is that it works as a filter for the desired beam type and energy. This is because the magnetic field is configured according to Eq. (2.1) to provide the correct bending of 90° to particles of the specific charge q, mass m and velocity $\vec{v}$ of the desired particle type and energy. The accelerated particles are non-relativistic, $E_{\text{kin}} \ll E_{\text{mass}}$, and the velocity is related to the energy by the classical formula

$$v = \sqrt{\frac{2E}{m}} \ . \tag{2.2}$$

In this experiment, a 38 MeV ^{3}He beam is extracted from the cyclotron and guided towards the ^{108}Pd target located within the "CACTUS/SiRi" target station, where the reactions and measurements take place. The detector systems situated here will be described in Sec. 2.1.4.

2.1.2 The cyclotron

The cyclotron consists of a large electromagnet composed of two circular, paralleled magnet poles designed to provide an approximately homogenous magnetic field $\vec{B}$ in a gap between them, where the acceleration electrodes are situated. The dimensions of the magnet system are $3.1\,\mathrm{m}\times1.3\,\mathrm{m}\times2.02\,\mathrm{m}$ ($l \times w \times h$), where the diameter of the magnet poles is $d = 1.3\,\mathrm{m}$. In order to obtain sufficient vertical focusing, the magnet poles are segmented in three sectors of a valley and a hill, i.e. sectors which results in larger and smaller gaps respectively when the poles are joined. The valley- and hill gaps are $h = 18\,\mathrm{cm}$ and $10\,\mathrm{cm}$ respectively. The maximum average magnetic field is $B = 1.7\,\mathrm{T}$, and the extraction radius, i.e the edge of the homogenous magnetic field, is $r = 51\,\mathrm{cm}$.

The particle acceleration system is sandwiched between the magnet poles. It consists of two accelerating electrodes (dee's), and two grounded sections (dummy dee's). The dee's and dummy dee's are equally dimensioned circular sections covering 90° each, and are positioned symmetrically to form a complete circle of 360°. They are basically copper casings with open sides facing eachother, and are separated by small, parallel gaps composing four acceleration gaps. A basic sketch of the composition of the cyclotron is illustrated in Fig. 2.2.

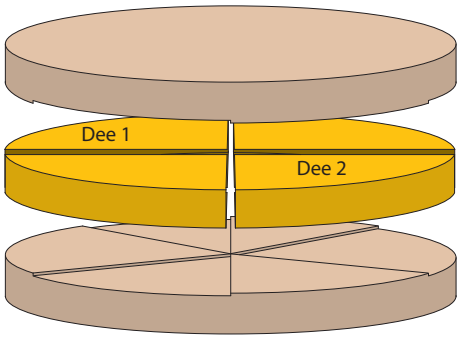

Figure 2.2:
A basic sketch of the composition of the MC-35 cyclotron. The distance between the components are exaggerated for clarity.

Both dees are connected to high frequency oscillating circuits, and a rapidly varying electric field $\vec{E}$ can be applied across the acceleration gaps. The particles to be accelerated are provided by an ion source in the center of the cyclotron and are sent horizontally into dee 1. The ions carry a charge q and have a horizontal velocity $\vec{v}$ due to the injection, and are thus according to Eq. (2.1) affected by the Lorentz force in the vertical magnetic field $\vec{B}$ between the cyclotron magnets.

This forces them to follow a circular trajectory, which leads the charged particles towards the first acceleration gap, where they will be accelerated by the electric force in the direction of the applied electric field,

$$\vec{F} = q \cdot \vec{E} \ . \tag{2.3}$$

Particles which enter the first gap in phase with the oscillating electric field will be successfully accelerated throughout the entire acceleration process, which is described in the following.

The dee's are operated in 180° phase shift, in a mode called push-pull. In this mode, a particle is accelerated four times during a revolution, and these steps are illustrated in Fig. 2.3. A positively charged particle injected by the ion source in phase with the oscillating circuits, arrives at the first gap when the voltage of dee 1 is positive and rising, and reaches the first dummy dee when this voltage is at maximum value. That is, the particle experiences an increasing, accelerating electric field in the acceleration gap. The accelerated particle traverses the dummy dee and enters the next gap when the voltage of dee 2 is negative and rising, and reaches dee 2 when this voltage is zero. In this case, the particle experiences a decreasing, yet accelerating electric field in the acceleration gap. When the particle reaches the next gap, the procedure repeats itself with dee 2 in place of dee 1, and so on until full acceleration has been acheived and the particle is extracted, which is performed by an electric field applied by the deflector. The mode is called push-pull because the particle is first pushed by the preceding dee and then pulled by the following dee with respect to the grounded dummy dee in each sequence of the procedure. There are two such sequences in a full revolution. As already mentioned, particles accelerated at the OCL obtain only non-relativistic energies. In this case, the characteristics of the particles motion during acceleration is increasing radius of the circular trajectory, and a constant time of revolution. The electrode frequency f of the oscillating circuit then has to correspond to the angular frequency ω of the particles to be accelerated. The relation between the angular frequency ω and the centripetal acceleration a is

$$\omega = \frac{v}{r} \ , \tag{2.4a}$$

$$a = \frac{v^2}{r} = \omega v \ , \tag{2.4b}$$

where r is the radius of the circular motion. Combining this relation with the definition of force and Eq. (2.1), the angular frequency can be described by

$$F = ma = qvB \Rightarrow \omega = \frac{qB}{m} \ . \tag{2.5}$$

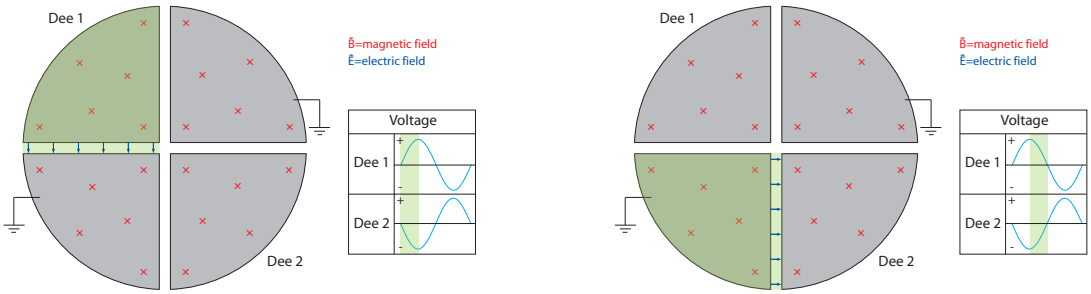

a) Particles are pushed by dee 1.

b) Particles are pulled by dee 2.

c) Particles are pushed by dee 2.

d) Particles are pulled by dee 1.

Figure 2.3: The acceleration procedure for particles in phase with the electrode frequency. The particles are accelerated by the electric force in the gaps, and the procedure is shown for a full revolution.

The vector notation can be omitted in Eq. (2.5) because the velocity $\vec{v}$ is perpendicular to the magnetic field $\vec{B}$. The electrode frequency can then be expressed as

$$f = \frac{\omega}{2\pi} = \frac{qB}{2\pi m} \,, \tag{2.6}$$

which is the so called cyclotron frequency. As seen in Eq. (2.6), this is determined by the magnetic field of the cyclotron and the type of particle to be accelerated. The strength of the magnetic field is again determined by the type and desired energy of the particles to be accelerated, because they have to be close to the extraction radius at this energy, and the Lorentz force has to act on them correspondingly.

The particles follow a spiral shaped path during the acceleration process in the cyclotron, from the ion source in the center to the edge of the magnetic field where they are extracted. From here, the accelerated particles are transported towards the target in order to produce the desired reactions.

Information and details about the cyclotron were found in the MC-35 manuals

located at OCL.

2.1.3 The nuclear reactions

The nuclear reactions of interest in this experiment are (^{3}He, α) and (^{3}He, ^{3}He'), which are used to investigate the properties of the nuclei ^{107,108}Pd respectively. In the reaction ^{108}Pd(^{3}He, α)^{107}Pd, an incoming ^{3}He particle collides with a ^{108}Pd nucleus in the target foil, picks up a neutron, and results in an outgoing α particle leaving a ^{107}Pd nucleus behind. In the reaction ^{108}Pd(^{3}He, ^{3}He')^{108}Pd, an incoming ^{3}He particle is inelastically scattered against a ^{108}Pd nucleus in the foil, providing an energy transfer to the nucleus during the collision. However, note that elastic collision is more probable, but does not excite the nucleus and is thus not of interest.

By measuring the energies of the ejectiles of the reactions, one can calculate the excited states obtained by the corresponding nuclei during the collisions, since the energy of the incoming ^{3}He particles is known. If an ejectile is detected, the subsequent γ-emissions of the de-excitations are also measured, and these measurements are combined to provide a picture of the excited states and the de-excitation pattern of the nuclei.

2.1.4 The detectors

The two detector systems "SiRi" and "CACTUS" have been used in this experiment, and will be described in this section. They are mounted about the target in order to measure particle energy[1] and γ-ray energy[2] of the ejectiles and γ-rays following reaction events.

SiRi is an acronym from silicon ring, and is a composite system consisting of 8 trapezoidal shaped silicon detector modules put together to form an approximate ring around the target, as shown in Fig. 2.4a). Each of these modules consists of a 1550 μm thick E detector with a 130 μm thick ΔE detector in front. The ΔE detectors are segmented into 8 curved strips which cover scattering angles between 40°-54°, i.e. one strip covers 2°, where the scattering angle is measured relative to the beam direction. A segmented front detector is illustrated in Fig. 2.4b). In front of the detector modules, a 10.5 μm thick aluminum foil is placed to shield the ΔE detectors from δ-electrons. The SiRi system is located inside the target vacuum chamber, with the center of the detector modules in a distance of 5.0 cm from the target, as shown in Fig. 2.4c). Table 2.1 provides a tabulation of the maximum energy deposition possible by different particles in the ΔE detector (column 2), and

[1] SiRi
[2] CACTUS

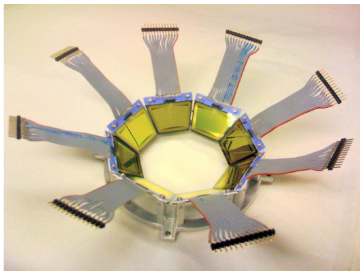

a) The composite SiRi detector system.

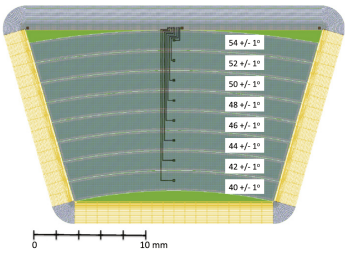

b) The segmented ΔE detector.

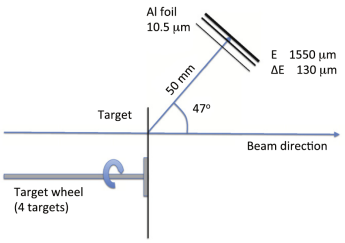

c) The position of SiRi in the target chamber.

Figure 2.4: The SiRi detector system. The figures are taken from [7].

in the complete module (column 3) with corresponding ΔE and E values (column 4 and 5 respectively). The 38 MeV ^{3}He beam used in this experiment results in ejectiles of $(\Delta E + E)_{\max} \approx 48$ MeV and ≈ 37 MeV for α and ^{3}He, respectively, at the angles covered by SiRi. As seen from column 3 in Tab. 2.1, these values are well below the maximum values for the respective particles.

Particle type	$\Delta E_{\max}$	$(\Delta E + E)_{\max}$	ΔE	E
p	3.7	16.5	0.7	15.8
d	4.9	22.3	1.0	21.3
t	5.7	26.5	1.2	25.3
^{3}He	13.4	58.3	2.6	55.7
α	15.0	65.9	2.9	63.0

Table 2.1: The energy characteristics of the SiRi detector modules, all energies are given in MeV. Numbers taken from [7].

CACTUS is the name of a detector system consisting of 28 NaI γ-ray detectors arranged in a spherical distrubution around the target. The detectors are of dimensions 5"×5" and have a total efficiency of ≈15%, and an energy resolution of ≈6% FWHM at the γ-ray energy of 1332 keV. They are shielded by 10.0 cm thick, conical lead collimators with an aperture of ϕ =70 mm at the front end, i.e the end pointing towards the target. The CACTUS arrangement envelops the target, and the detector front ends are positioned 22.0 cm from the center of it. The detector system has been named after its appereance, which can be seen in Fig. 2.5.

Both detector systems are designed to measure the energy deposited by ionizing radiation, which as its name states, carries enough energy to ionize atoms in matter in which it interacts. There are two fundamental types of ionizing radiation, i.e. directly- and indirectly ionizing. Directly ionizing radiation is caused by charged particles, which in addition to collisions, interact directly with atomic electrons through the Coulomb force. The scalar form of the Coulomb force is

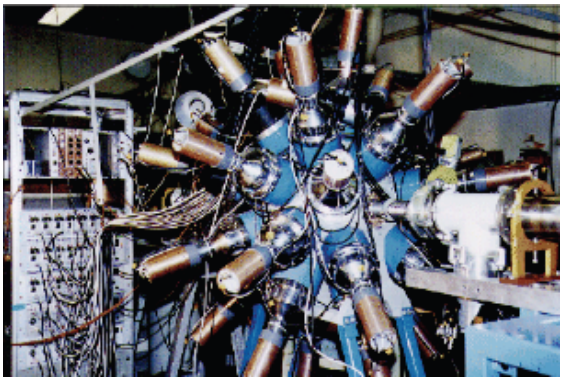

Figure 2.5:
CACTUS as seen from the outside. The appereance resembles a cactus, hence its name.

given by

$$F = \frac{1}{4\pi\epsilon_0}\frac{q_1 q_2}{r^2} \ , \tag{2.7}$$

where ϵ_0 is the electric constant, q_1 and q_2 is the charges of the interacting particles, and r the distance between them. The energy deposition of a charged particle per unit length in a material can be calculated by [9]

$$-\frac{dE}{dx} = 2\pi N_a r_e^2 m_e c^2 \rho \frac{Z}{A}\frac{z^2}{\beta^2}\left[\ln\left(\frac{2m_e\gamma^2 v^2 W_{\max}}{I^2}\right) - 2\beta^2 - \delta - 2\frac{C}{Z}\right] \ , \tag{2.8}$$

which is the Bethe-Block formula. The variables of Eq. (2.8) are explained in Tab. 2.2.

N_a:	Avogadro constant	v:	speed of the ionizing particle
r_e:	electron radius	β:	v/c
m_e:	electron mass	γ:	$1/\sqrt{1-\beta^2}$
c:	speed of light in vacuum	$W_{\max}$:	maximum energy transfer in a collision
ρ:	density of the material	I:	mean excitation potential
Z:	atomic number of the material	δ:	density correction
A:	mass number of the material	C:	shell correction
z:	charge of the ionizing particle		

Table 2.2: Variables of the Bethe-Block formula.

Indirectly ionizing radiation on the other hand, is caused by electrically neutral particles which ionize only by collision with atomic electrons. However, the electrons are knocked off and are in turn directly ionizing. In this experiment the

indirectly ionizing radiation of interest is caused by γ-rays, which has three basic interactions with matter. That is, photo-electric effect, compton scattering and pair-production.

In the event of photo-electric effect, a γ-ray collides with an atomic electron, is absorbed, and gives all of the energy to this electron. The kinetic energy of the electron is then equal to the energy of the γ-ray minus the electron binding energy, and it deposits this energy according to Eq. (2.8) since it is directly ionizing. In order to conserve momentum, this process can only take place for bound electrons since the recoil momentum has to be absorbed by a heavy body at low kinetic energy cost. Usually, the true γ-ray energy is measured when this process occurs, since the electron binding energy is relatively small. Hence, the photo-electric effect is the most desirable process with respect to energy measurements.

Compton-scattering is scattering of γ-rays from essentially free electrons. This situation arises when the binding energy of the electrons is much smaller than the γ-ray energy. The incoming γ-ray collides with a "free" electron, transfers a part of its energy and is scattered in an angle corresponding to the kinematics of the collision. The electron will then deposit the received energy according to Eq. (2.8), and the scattered γ-ray will continue until it either interacts again, or escapes the material altogether. A γ-ray can never transfer all of its energy, E_γ, in a Compton scattering event. This is because the energy transfer is limited by the maximum recoil energy described by

$$T_{\max} = E_\gamma \left(\frac{2\eta}{1+2\eta} \right) \ , \tag{2.9}$$

where $\eta = E_\gamma / m_e c^2$. Therefore, this interaction process is undesired since it may lead to γ-rays escaping the detector, resulting in a broad distribution ranging from 0 to $T_{\max}$ in the measured energy spectrum for γ-rays of a specific energy. There is a sharp drop in such a measured γ-ray energy spectrum at the maximum energy $T_{\max}$, which is commonly referred to as the *Compton edge*.

Pair-production becomes physically possible at γ-energies above 1.022 MeV. In this process, the incoming γ-ray is totally absorbed, and a part of the energy is used for the creation of an electron-positron pair. The minimum energy limit of the process is determined by the mass of the constituents of the pair, i.e twice the electron mass of $m_e = 511\,\mathrm{keV/c^2}$. Excess energy is distributed as kinetic energy between the created electron and positron. In order to conserve momentum, this process must take place in the potential of a third body, which generally is an atomic nucleus. The electron and positron are directly ionizing and the energy deposition follows Eq. (2.8). However, when the kinetic energy of a positron is low enough, it is annihilated by an electron, leading to the emission of two 511 keV photons in opposite directions. One, or both, of these photons may escape the

detector material along with the respective energy information, and might cause the measured energy of a γ-ray to be 511 keV or 1022 keV below the true value.

The cross sections of these interaction processes have a dependence of Z^4, Z, and Z^2 for photo-electric effect, compton scattering, and pair-production, respectively, where Z is the number of protons of the matter in which the interactions take place. This implies that one should choose a high Z-value material in order to get an energy efficient γ-ray detector, because of the correspondingly high cross sections for γ-ray interaction processes.

The SiRi detector system is designed to measure the energy of charged particles, i.e. directly ionizing radiation. The system consists of silicon semi-conductor detectors which are based on the creation of electron-hole pairs in the material, and the number of such pairs to be proportional to deposited energy. The electron-hole pairs created in the sensitive volume of the detectors, i.e. a reverse biased pn-junction, are collected by the electric field and measured by a charge sensitive pre-amplifier which gives the output signal. The advantage of silicon semi-conductor detectors is the relative small amount of energy required to create an electron-hole pair, i.e. $w = 3.62\,\text{eV}$ for Si at 300 K [9]. The required energy w is also independent of the type and energy of the ionizing radiation. Another great advantage is that no cooling is nescessary. If a particle deposits all of its energy within the sensitive volume of a detector, the detector response will be linearly proportional to the particle energy E. However, there will be some recombination of the electron-hole pairs before they are collected by the electric field, so the detector has some collection efficiency n. The collected charge due to an ionizing charged particle with energy E deposited in the sensitive volume is then

$$Q = \frac{nE}{w} \ , \tag{2.10}$$

and the measured voltage of the signal is accordingly

$$V = \frac{nE}{wC} \ , \tag{2.11}$$

where C is the capacitance of the sensitive volume. The amplitude of the signal is thus linearly proportional to the energy of the ionizing particle, as long as the energy is deposited within the sensitive volume. More details about semi-conductor detectors can be found in [9].

CACTUS consists of NaI(Tl) scintillation detectors, where NaI(Tl) is an inorganic scintillation crystal doped by Tl. This crystal emits photons in a specific energy range whenever it is struck by ionizing radiation, i.e. it scintillates, and the intensity of the emitted photons depends on the amount of energy deposited. The detector crystal is connected to a PMT[3] which converts the emitted photons

[3]Photomultiplier tube

to measurable electric signals. The scintillation photons are first converted to photo-electrons by a photo-sensitive cathode. These electrons are in turn accelerated down a potential ladder of several dynodes held at higher and higher positive voltage. Each time an incoming electron hits a dynode, a number of secondary electrons are released and accelerated towards the next dynode. This is a multiplicative process, resulting in a measurable electric current to be produced at the anode. The number of electrons reaching the anode depends on the number of scintillated photons, which again depends on the amount of energy deposited in the detector material. Above some minimum energy, this relation is linearly proportional, and by measuring the current of the output signal, one gets a measure of the deposited energy. Note that the full energy of the ionizing radiation has to be deposited in the detector material in order to get the correct energy information. The NaI(Tl) crystal has a relatively high Z-value, and is thus suitable for detecting γ-rays with the purpose of measuring their energy.

2.1.5 Signal processing and data acquisition

Signal processing from the SiRi detector system is done by four pre-amplifiers for the 64 ΔE detector strips, handling 16 strips each, and one pre-amplifier for the 8 E detectors. The pre-amplifiers are of type Mesytec MPR-16, and the output is differential signals which are transmitted to Mesytec STM-16 modules. They contain spectroscopy- and timing filter amplifiers, and a leading-edge discriminator.

The data acquisition is started by the logical "OR" signal of the discriminator outputs of the E-detectors in SiRi, and is stopped by a slightly delayed signal from a detection in one of the 28 NaI detectors in CACTUS. In other words, the acquisition is started by a particle detection in SiRi and stopped by a γ-ray detection in CACTUS. The events are in reality happening in coincidence, but the stop signal is briefly and deliberately delayed by $\approx 522\,\text{ns}$ in order to obtain a small time frame where measurements are accepted. The coincident γ-rays detected in CACTUS are later sorted offline, by only accepting the signals arriving with the known time delay. In this way, only the γ-rays in coincidence with the detected particles are extracted. Conversion from analog to digital signals is performed by ADC's from CAEN (mod.785) and Mesytec (MADC-32), and from time to digital signals by a TDC from CAEN (mod.775). The data acquisition system is placed in a VME module rack, and is controlled by software running on a CES8062 CPU. The data is transferred to a Linux-computer by a CAEN VME USB module (mod.1718).

As a summarizing reminder, the recorded energy information is the ΔE and E of the particles measured by SiRi, and the coincident γ-ray energies detected by CACTUS.

2.2 Offline data treatment

Small differences in the response of the detectors is inevitable due to manufactural issues regarding the detector material and the electronics. Therefore, one has to calibrate the measured data of each detector to known values, in order to align the experimental energy spectra. It is also nescessary to correct the effects of *walk*, and sort the data by the reactions of interest. All these procedures will be described in this section.

2.2.1 Calibration

Calibration of the measured particle energy spectra is done by fitting $\Delta E/E$-plots to known theoretical values, which are calculated by the software *OCL SiRi Kinematics Calculator* [10]. The software is based on Eq. (2.8), the specifics of the detectors, the type and energy of the ejectile, the type of target nucleus, and the thickness of the target foil. A plot of the calculated values for the reactions of interest in this experiment is shown in Fig. 2.6. In the experimental data, peaks corresponding to the energies shown in Tab. 2.3 have been used as reference points in the calibration.

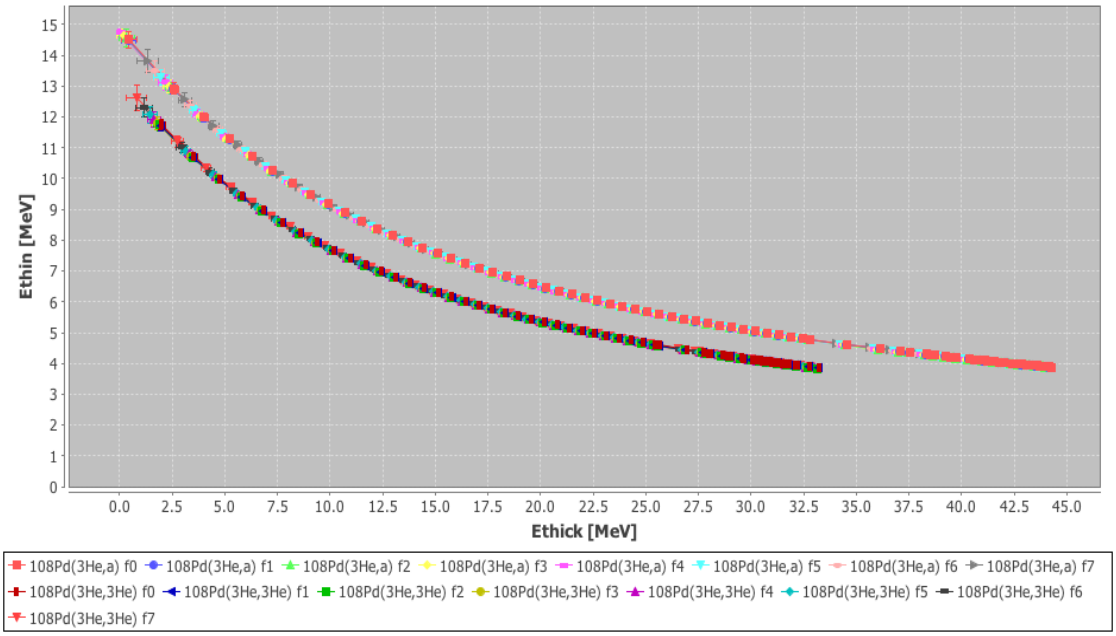

Figure 2.6: Values calculated and plotted by the OCL SiRi Kinematics Calculator [10]. Only the values corresponding to the reactions of interest are plotted, with ΔE along the y-axis and E along the x-axis.

Nucleus	E_x of the nucleus	Particle	E	ΔE
^{108}Pd	0 keV	^{3}He	~ 33 MeV	~ 3.9 MeV
^{107}Pd	214.9 keV	α	~ 44 MeV	~ 3.9 MeV
^{12}C	9641 keV	^{3}He	$\sim 14.6 - 18$ MeV	$\sim 5.7 - 6.4$ MeV

Table 2.3: The energy in E and ΔE of the peaks used for calibration. The numbers are calculated by the OCL SiRi Kinematics Calculator [10], and are here given as approximate since the energy is dependent of the angle and are slightly different for the 8 strips.

As mentioned, the response of the detectors is linear, and the energy of the particle in the measured spectrum is determined by

$$E(x) = a + b \cdot x \ , \tag{2.12}$$

where a is the energy in channel 0 of the spectrum, b is the energy per channel, and x is the channel number. The calibration is performed by determining the coefficients a and b in such a way that $E(x)$ at the reference peaks in the experimental data match the theoretical values predicted by the software [10]. This goes for calibration of both ΔE and E axes. In order to obtain a good calibration, peaks with some distance within the region of interest should be chosen as reference points.

The experimental $\Delta E/E$-plots before and after calibration are shown in Fig. 2.7. Unfortunately there was something wrong with the response of the 8th detector-module of SiRi, for which the measurements had to be excluded. Other than reducing the total number of measurements by $\approx \frac{1}{8}$, the final results of the analysis will not be affected. This is because the γ-rays in coincidence with detection in detector 8 are excluded as well, since the start signal for accepting these measurements is never issued. To illustrate the problem of detector module 8, a $\Delta E/E$-plot with its measurements included is shown in Fig. 2.8. At energies $E < 14$ MeV (x-axis), the deviation becomes evident. It is also slightly noticeable at energies $E > 30$ MeV.

The advantage of arranging the measured data in $\Delta E/E$-plots, is that in addition to measuring the total energy $E_{\text{tot}} = \Delta E + E$, one can also distinguish between the different particles. This is because of the dependence of mass and charge in the energy deposition of a particle, according to Eq. (2.8), and the ΔE detectors give a measurement of this difference. In other words the ΔE detectors are in principle measuring $-\frac{dE}{dx}$, i.e. the left hand side of Eq. (2.8). The data can then be sorted by the different reactions by gating on the corresponding ejectile, i.e. extracting data corresponding to the $\Delta E/E$-curve of the respective ejectile only.

The energy calibration of the γ-ray energy spectrum is performed by comparing peaks in the experimental spectra to known values [11], and using Eq. (2.12) for

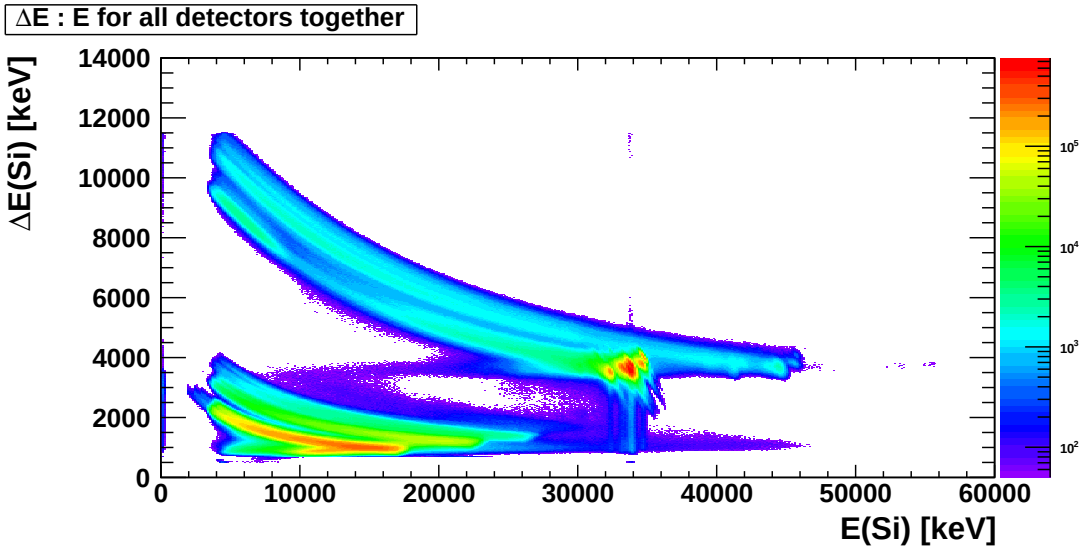

a) Before calibration.

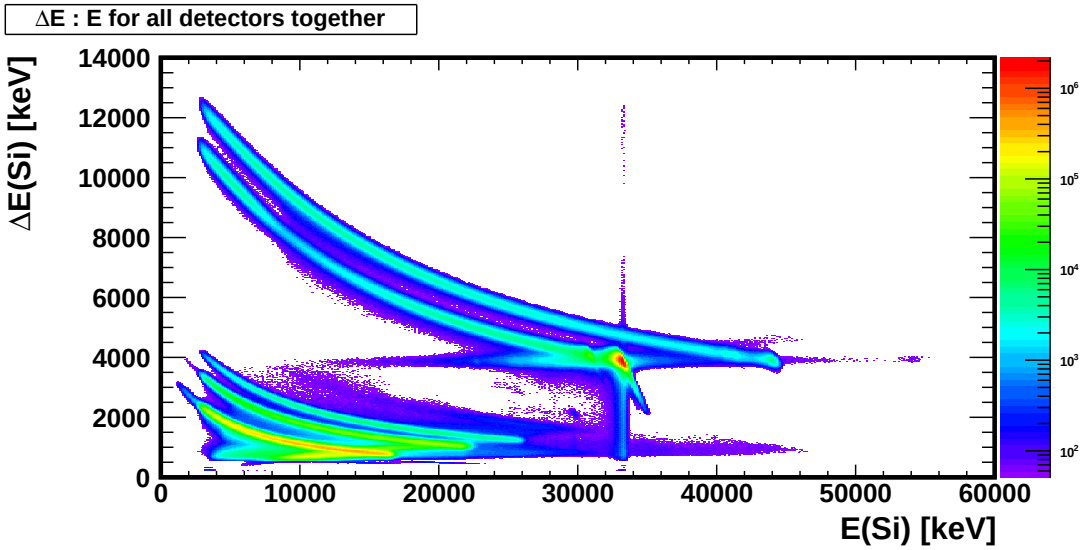

b) After calibration.

Figure 2.7: Before and after calibration of the detectors. The figures show $\Delta E/E$-plots, with ΔE along the y-axis, E along the x-axis and number of counts on the z-axis (in colors). After the calibration, curves from the different particles are clearly distinguishable: p, d, t, ^{3}He, and α, from the bottom left corner respectively. Also note the relative increase of counts after the calibration.

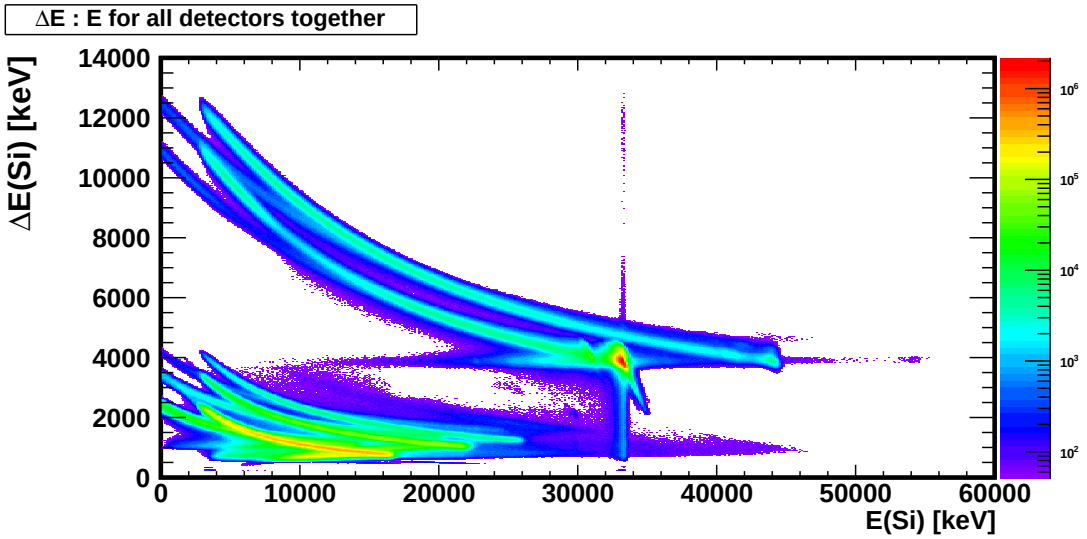

Figure 2.8: Measurements of the 8th detector module of SiRi is included in this $\Delta E/E$-plot. One can clearly see why data from this detector module has to be omitted. Data from detector module 8 deviates from the rest for $E < 14$ MeV.

calibration. Calibration is performed by using γ-ray spectra from the ^{12}C data, because they contain nice peaks at γ-ray energies of 511 keV and 4.4 MeV, and is performed individually for all the 28 NaI detectors.

2.2.2 Sorting by particle type

The gating on a specific ejectile, and thus a certain reaction, is performed by extracting data only from the corresponding $\Delta E/E$-curve. Using Eq. (2.8) with input of the experimental- and empirical range data for the particle in question, one can calculate the thickness of the ΔE detector. Calculations by experimental data of the desired particle will then be distributed around the known true value of the ΔE detector thickness, which is $\approx$130 μm, and this distribution identifies data of the desired particle. This is demonstrated for ^{3}He in Fig. 2.9. The limits of the gating window are then put appropriately about the peak corresponding to the desired particle, and only data within this window is extracted and used in the further analysis. When a particle gate has been applied, only the corresponding coincident γ-ray measurements are extracted as well.

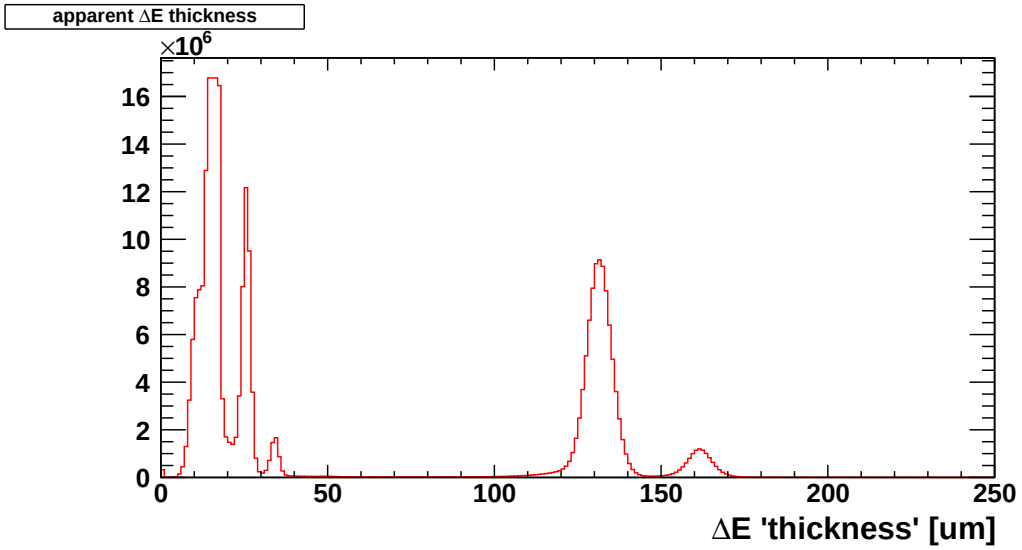

Figure 2.9: Calculated thickness of the ΔE detector using the empirical range curve for ^{3}He. *The peak centered about ∼130 µm, i.e. the true thickness of the ΔE detector, consists of data due to detected* ^{3}He *events. The other peaks are due to other ejectiles, which wrongly estimates the thickness because the input parameters are intended for* ^{3}He.

2.2.3 Energy-time correction

Leading edge discriminators are used for discrimination between noise and useable signals. Unfortunately, the time spectrum is then dependent on the energy of the measured particles and γ-rays. The length of a time window, which is determined by a start signal from SiRi and the corresponding stop signal from CACTUS, is thus not constant and has to be corrected for. This is a problem called *walk*, and is because of the leading edge discriminators triggering the start- and stop signals have a lower threshold for the acceptance of signals, and the rise time of the input signals varies with energy. This means that a signal of higher amplitude will be detected as happening before a simultaneous signal of lower amplitude, because of their different rise times and corresponding time of crossing the lower threshold. The situation is depicted in Fig. 2.10, which demonstrates that signals of higher energy events will cross the lower threshold of the discriminators faster than signals of lower energy events. To correct for this effect, the function

$$t(x) = 200 + a + \frac{b}{(x+c)} + d \cdot x \ , \tag{2.13}$$

is fitted to the measure time vs. energy curve. Here, t is the channel number corresponding to time and x is the channel number corresponding to energy. The

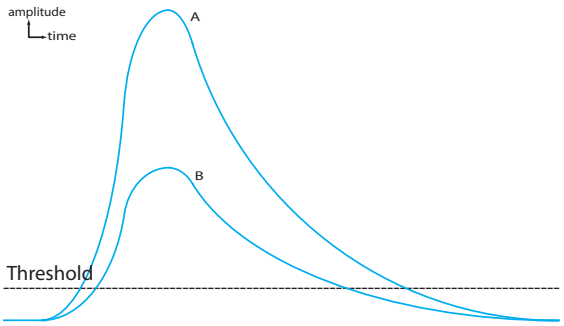

Figure 2.10:
The origin of walk. In reality event A and B are coincident, but due to walk it would seem like event A is happening before event B.

coefficients found in the fit are then used to counteract the walk, and the coincidence time pulses are aligned to lie in channel 200, hence the addition of 200 in Eq. (2.13). Correction of the CACTUS γ-ray time spectrum, when gated on ^{3}He, is illustrated in Fig. 2.11.

The correction of the SiRi time spectrum is performed in the exact same way, and is aligned with the CACTUS time spectrum at channel 200. For the extraction of coincident γ-rays only, gate limits are appropriately placed about the peak in channel 200 of the time spectrum. The other peaks observed in the time spectrum, are from earlier and later beam pulses that occurred within the total time frame, but for which no triggering particle detection was made. The measurements within these peaks thus represent random coincidences of background radiation, and can be subtracted from the real coincidence γ-ray spectra by gating by the same limit interval about one of those peaks and subtracting the resulting spectra.

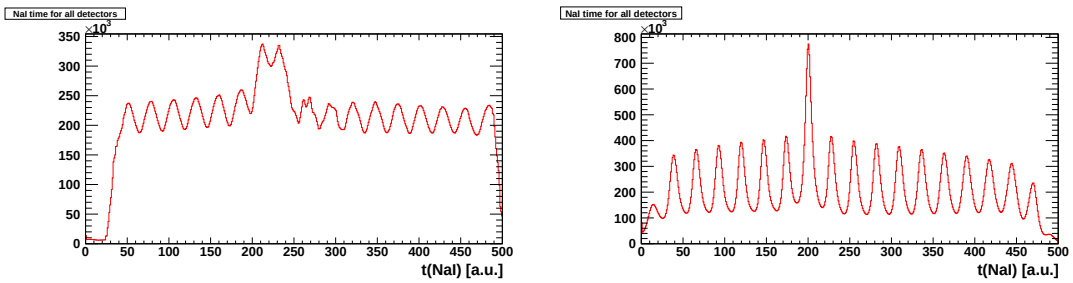

a) Before correction. *b) After correction.*

Figure 2.11: Correction of walk is important in order to obtain a good resolution of the time spectrum. The improvement of the resolution is absolutely obvious.

2.2.4 Coincidence matrices

After the calibration and sorting of data have been performed, matrices of coincidence measurements can be arranged. Because the energy of the accelerated particles is known, the excitation energy E_x obtained by a nucleus in a reaction event can be calculated from the measured energy of the ejectile of the reaction. The coincident γ-ray spectra corresponding to these excitation energies are arranged in matrices of elements (E_γ, E_x), where E_γ is the γ-ray energy. This gives a histogram of counts filling data channel bins representing E_x along the y-axis, and corresponding E_γ in channel bins along the x-axis. All the experimental spectra used in further analyses are arranged in such a way. The coincidence matrices are the basis of the analyses, and the calibrated (E_γ, E_x) matrices for the two nuclei investigated in this experiment are depicted in Figs. 2.12 and 2.13. The matrices for ^{107,108}Pd are obtained by gating on the ejectiles α and ^{3}He respectively.

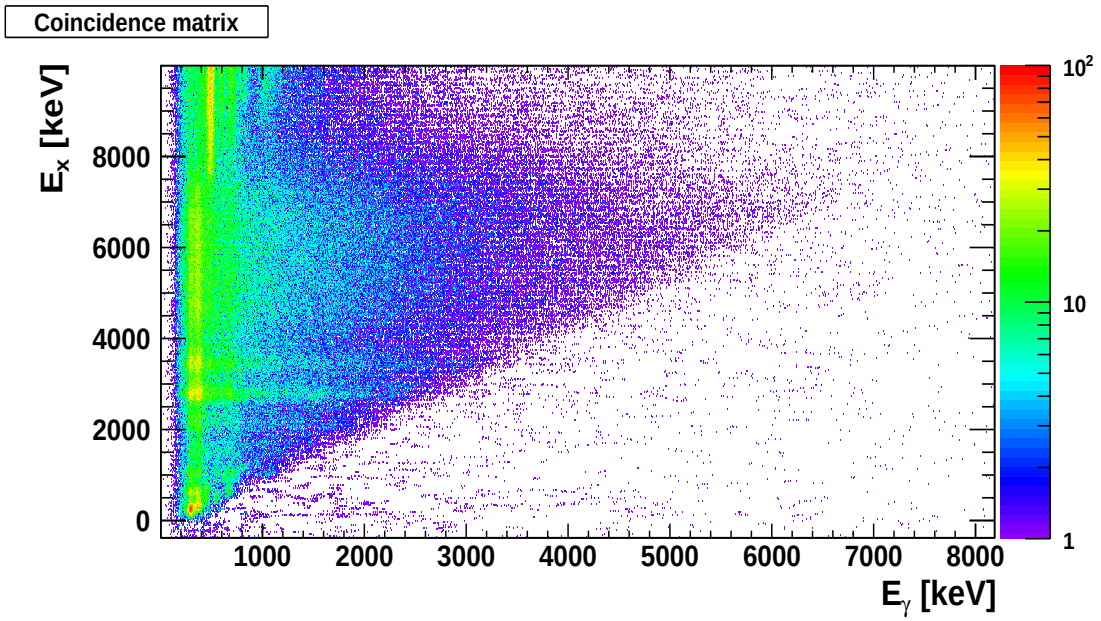

Figure 2.12: Coincidence matrix of ^{107}Pd*, which is obtained by gating on* α*. The number of counts are expressed in colors.*

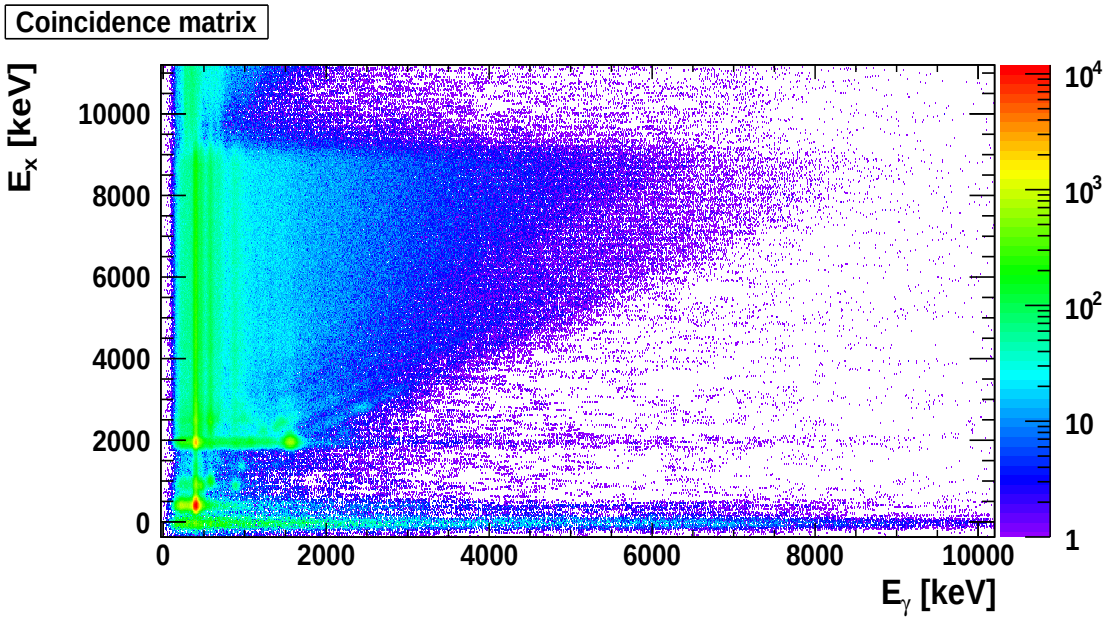

Figure 2.13: Coincidence matrix of ^{108}Pd*, which is obtained by gating on* ^{3}He*. The number of counts are expressed in colors.*

Chapter 3

The Oslo method

This chapter explains the methods used for extraction of data from the experimental coincidence matrices. Also, the various assumptions and theoretical considerations are discussed.

3.1 Unfolding of γ-ray spectra

A measured spectrum of γ-rays of a specific energy will have a broad energy distribution due to different interaction processes with the detector material, i.e. photoelectric effect, compton scattering, pair production, annihilation radiation and backscattering in the surroundings. The effects of these processes in the γ-ray energy spectrum are listed in Tab. 3.1. A process called unfolding must be applied to the γ-ray spectrum in order to subtract undesired contributions of the different processes, so extraction of useful information can be performed. This section will explain the steps of this process.

First, one has to obtain the detector response function which describes how

Interaction process	Characteristics	Measured E_γ
Photoelectric effect	*Peak structure*	E_γ
Compton scattering	*Broad distribution*	$[0,\ T_{\max}]$
Pair production	*Peak structures*	$E_\gamma - 511\,\mathrm{keV}$, $E_\gamma - 1022\,\mathrm{keV}$
External annihilation radiation	*Peak structure*	$511\,\mathrm{keV}$

Table 3.1: Impact of the different interaction processes on γ-ray energy spectra when a γ-ray of energy E_γ is measured. The maximum energy for Compton scattering is given by Eq. 2.9, and pair production comes into account for $E_\gamma \geq 1022\,\mathrm{keV}$.

the energy of an incident γ-ray is deposited in the detector material. The response function depends on the mentioned interaction processes, which all have different energy dependent cross-sections. The energy deposition is measured experimentally at various known monoenergetic γ-lines, and the response function is obtained by interpolating between these points according to the method described in [12]. The response function gives the relation between the deposited energy E in the detector and the energy E_γ of an incident γ-ray, and is denoted

$$R(E, E_\gamma) \ . \tag{3.1}$$

When the response function is known, the unfolding procedure can be applied to a measured γ-ray spectrum. This is done by the *folding iteration method* which takes advantage of the fact that folding is a fast and simple process, as described in [12] and its references. The folding can be expressed as

$$f = \mathbf{R}u \ , \tag{3.2}$$

where f and u is the folded and unfolded γ-ray spectrum respectively, and $\mathbf{R}$ is the response matrix. The matrix is arranged in such a way that element $R_{i,j}$ gives the response in channel i when energy corresponding to channel j is detected. The iteration method is carried out in a few simple steps, which is repeated until the folded γ-ray spectrum f looks like the observed γ-ray spectrum r. The steps of the procedure will be explained in the following.

First, one has to choose a trial spectrum u^0 to fold, and this is generally put to be equal to the observed spectrum, i.e. $u^0 = r$. Then, the trial spectrum is folded according to Eq. (3.2) and provides the first folded γ-ray spectrum f^0. A new trial spectrum is constructed by adding the difference between the observed and the folded spectrum to the old trial spectrum,

$$u^1 = u^0 + (r - f^0) \ . \tag{3.3}$$

The new trial spectrum is then folded, and the process is repeated until $f^i \approx r$, where i is the number of iterations. The unfolded γ-ray spectrum is then given by the corresponding u^i. In order to acheive the best unfolding result with this method, the resolution (FWHM) of the response matrix used in the folding should be set to half the value of the experimentally observed response obtained by Eq. (3.1). This is done to prevent large negative undershoots and artificial peaks around prominent peaks in the unfolded γ-ray spectrum, which arise from reasons explained in [13].

After the *folding iteration method* has provided an unfolded γ-ray spectrum u, the *Compton subtraction method* [12] is applied to produce a much less fluctuating γ-ray spectrum. This is carried out by first defining a new spectrum v, which is

to be the observed γ-ray spectrum without the compton contribution. The new spectrum is described by the unfolded γ-ray spectrum as

$$v(i) = p_f(i)u(i) + w(i) \ , \tag{3.4}$$

where i is the channel bin number, $p_f(i)u(i)$ is the full energy contribution, and $w(i) = u_s(i) + u_d(i) + u_a(i)$ is the contribution from single- and double escape and annihilation in the surroundings respectively. These contributions are described by

$$u_s(i - i_{511}) = p_s(i)u(i) \ , \tag{3.5}$$

$$u_d(i - i_{1022}) = p_d(i)u(i) \ , \tag{3.6}$$

$$u_a(i_{511}) = \sum p_a(i)u(i) \ , \tag{3.7}$$

where i_{511} and i_{1022} are the channel bin numbers corresponding to the energies 511 keV and 1022 keV respectively, and p denotes the corresponding probability of the interaction. The Compton background spectrum c is extracted by subtracting the newly defined spectrum from the experimentally observed γ-ray spectrum,

$$c(i) = r(i) - v(i) \ . \tag{3.8}$$

This spectrum contains no peak structures and can be strongly smoothed without loss of important information. The new, and less fluctuating unfolded γ-ray spectrum is obtained by combining Eqs. (3.4) and (3.8), and using the smoothed Compton background spectrum in place of c,

$$u(i) = [r(i) - c_{smoothed}(i) - w(i)]/p_f(i) \ . \tag{3.9}$$

The final step of the unfolding process is to correct for the energy dependent total γ-ray efficiency ϵ_{tot}, and obtain the final unfolded γ-ray spectrum

$$U(i) = \frac{u(i)}{\epsilon_{tot}(i)} \ . \tag{3.10}$$

Further details about the methods used in this section are found in [12] and its references.

The unfolding procedure is applied to the γ-ray spectra of the experimental (E_x, E_γ) coincidence matrices, and corresponding coincidence matrices of unfolded γ-ray spectra are thus obtained.

3.2 Extraction of first generation γ-ray spectra

The γ-decay from high excitation energies contains in general a cascade of γ-ray transitions. Experimentally, the individual γ-ray transitions in a cascade cannot be distinguished because of the fast timing of these processes, and the measured γ-ray spectra will consequently contain contributions from all generations of γ-rays in the cascade. In order to investigate the transitions by γ-rays originating from a certain level at high excitation energy, one has to extract a *first generation* γ-ray spectrum of this level, i.e the first γ-rays of the cascade. A method of this purpose has been developed [14], and will be explained in this section.

For the extraction method to be valid, it is assumed that the γ-decay patterns of the excited states are the same whether they are populated by a direct reaction, or by the γ-decay from a higher level. Arguments discussed in [15] support this assumption. In the unfolded (E_γ, E_x) coincidence matrix, a γ-ray spectrum is stored for each excitation energy bin. These spectra are denoted f_i, with $i = 1$ for the highest excitation energy bin included in the extraction. The first generation γ-ray spectrum h_i is estimated by

$$h_i = f_i - g_i \ , \tag{3.11}$$

where g_i is a weighted sum of all spectra of lower excitation energy,

$$g_i = \sum_{j=i+1}^{j} n_j w_j f_j \ . \tag{3.12}$$

The weighting factor n_j is determined so that the area of each spectrum f_j multiplied with n_j corresponds to the same number of cascades, and is found by *multiplicity normalization* [14]

$$n_j = \frac{M_j A(f_i)}{M_i A(f_j)} \ , \tag{3.13}$$

where M is the γ-ray multiplicity and A denotes the corresponding area of the spectrum. The γ-ray multiplicity for each excitation energy bin, denoted M_i, is calculated by the average total γ-ray multiplicity formula [16]

$$M_i = \langle M_i \rangle = \frac{E_i}{\langle E_\gamma \rangle} \ , \tag{3.14}$$

where E_i is the excitation energy represented by bin i and $\langle E_\gamma \rangle$ is the average γ-ray energy of the γ-ray spectrum corresponding to this bin. The weight w_j is unknown and represent the probability of decay from bin i to bin j. It can however

be found by a fast iteration process using the response function of the detectors. This is done by first applying a trial function of w_j which is used to deduce h_i, then h_i is unfolded and its area is normalized to 1. The new weighting function is then set to $w_j = h_i$, and these steps are repeated until the new and previous weighting functions are approximately equal.

After a sufficient amount of iterations, generally 10-20, matrices of first-generation γ-ray spectra are extracted from the unfolded (E_x, E_γ) coincidence matrices. The extracted matrices are naturally arranged in the same way.

3.3 Factorization and extraction

When the first generation γ-ray matrices have been obtained, the extraction of level densities and γ-ray strength functions can finally be performed. The matrices of first generation γ-ray spectra are denoted $\Gamma(E_x, E_\gamma)$ where E_x and E_γ are the excitation- and γ-ray energy data bins respectively. Above some minimum energy $E_{\gamma,\mathrm{min}}$, the matrices are normalized for each excitation energy bin, i.e. the area of the γ-ray spectra are normalized to unity for all E_x bins. The lower limit $E_{\gamma,\mathrm{min}}$ is decided on basis of the experimental data, due to a methodical problem which will be clarified later.

The probability of γ-decay from an initial state E_x to a final state E_f by a γ-ray of energy $E_\gamma = E_x - E_f$, is assumed to be proportional to the level density $\rho(E_f)$ at the final state and a γ-ray energy dependent transmission coefficient $\mathcal{T}(E_\gamma)$. The normalized first generation γ-ray matrices can then be factorized into

$$\Gamma(E_x, E_\gamma) \propto \mathcal{T}(E_\gamma)\rho(E_x - E_\gamma) \ , \tag{3.15}$$

and a theoretical approximation of the normalized first generation γ-ray matrices can be described by the normalized expression

$$\Gamma_{\mathrm{th}}(E_x, E_\gamma) = \frac{\mathcal{T}(E_\gamma)\rho(E_x - E_\gamma)}{\sum_{E_\gamma = E_{\gamma,min}}^{E_x} \mathcal{T}(E_\gamma)\rho(E_x - E_\gamma)} \ . \tag{3.16}$$

The factorization of Eq. (3.15) is valid when the excited state is fully formed before the occurrence of γ-decay, and that the relative decay probability is independent of how the state was formed, i.e that the γ-ray transmission coefficient is only dependent of γ-ray energy. This is according to the generalized Brink hypothesis [17]. The hypothesis is violated for reactions involving high temperatures and/or spin, and since the temperatures and spins populated in reactions at OCL is relatively low, the factorization and corresponding assumptions are believed to hold.

Unique functional forms of $\mathcal{T}(E_\gamma)$ and $\rho(E_x - E_\gamma)$ are derived by fitting Eq. (3.16) to the normalized experimental first generation γ-ray matrices by a least squares method described in [18]. The basic idea of this method is to minimize

$$\chi^2 = \frac{1}{N_{\text{free}}} \sum_{E_x=E_{x,\min}}^{E_{x,\max}} \sum_{E_\gamma=E_{\gamma,\min}}^{E_x} \left(\frac{\Gamma_{\text{th}}(E_x, E_\gamma) - \Gamma(E_x, E_\gamma)}{\Delta\Gamma(E_x, E_\gamma)} \right) , \tag{3.17}$$

where N_{free} is the number of degrees of freedom, and $\Delta\Gamma(E_x, E_\gamma)$ is the uncertainty of the experimental first generation γ-ray matrix. Unfortunately, there is an infinite set of equally good normalizations of the two extracted functions which reproduce $\Gamma(E_x, E_\gamma)$. All these solutions can be constructed by applying the transformation generators below to one arbitrary solution,

$$\tilde{\rho}(E_x - E_\gamma) = \rho(E_x - E_\gamma) A e^{\alpha(E_x - E_\gamma)} , \tag{3.18}$$

$$\tilde{\mathcal{T}}(E_\gamma) = \mathcal{T}(E_\gamma) B e^{\alpha E_\gamma} , \tag{3.19}$$

where A and B are normalization coefficients, and α is the slope of the functions. The transformation generators are proved in [18]. The next step would be to determine the most physical solution of Eqs. (3.18) and (3.19), and this is performed by determining the transformation coefficients A, B, and α by fitting the transformations to known data from previous experimental results.

The determination of A and α is performed by normalizing the extracted level density at low excitation energies, as well as at the neutron binding energy B_n. At low excitation energies, this is performed by comparing the extracted level density to the number of known levels per E_x bin. In the high energy region however, some considerations have to be taken into account before the normalization can be performed. First, the level density at the neutron binding energy has to be deduced, which is performed according to the following procedure.

In the BSFG[1] model, the total level density for all spins and parities is given by [19]

$$\rho(U) = \frac{1}{12\sqrt{2}\sigma} \frac{e^{2\sqrt{a(U-E_1)}}}{a^{1/4}(U-E_1)^{5/4}} , \tag{3.20}$$

where U is the excitation energy, a is the level density parameter, E_1 is the energy backshift parameter, and σ is the spin-cutoff parameter. Further, the spin dependent level density can be described by

$$\rho(U, J) = \rho(U) \left[\frac{(2J+1) e^{-(J+1/2)^2/2\sigma^2}}{2\sigma^2} \right] , \tag{3.21}$$

[1]Back-shifted fermi gas

where J denotes the spin of the nucleus. The braced part of Eq. (3.21) is the spin distribution $g(U, J)$ of the level density [22], and the spin-cutoff parameter is given by the following equation [19]

$$\sigma^2(U) = 0.0146A^{5/3}\frac{1+\sqrt{1+4a(U-E_1)}}{2a} \ . \tag{3.22}$$

In a neutron resonance experiment where I_t is the spin of the target nucleus and ℓ is the angular momentum of the neutron, the neutron resonance spacing D_ℓ can be written in terms of the spin dependent level density as

$$\frac{1}{D_\ell} = \frac{1}{2}\sum_j \rho(B_n, I_t + j) \ , \tag{3.23}$$

where j represents the component of the total angular momentum of the neutron $\vec{j} = \vec{\ell} + \vec{s}$, which can be in any of the possible configurations. Terms where $I_t < -(j + \frac{1}{2})$ have to be omitted since they provide a negative level density according to Eq. (3.21), and are thus non-physical. This situation might only occur if $\ell > 0$. The relation of Eq. (3.23) is justified by the fact that all levels with $J = I_t + j$ for $j \geq -(I_t + \frac{1}{2})$ is accessible in a neutron resonance experiment, and the fraction in front of the sum comes from the assumption that both parities contribute equally to the level density at the neutron binding energy. The total level density at B_n is found by combining Eqs. (3.21) and (3.23), and rearranging with respect to the level density,

$$\rho(B_n) = \frac{2}{D_\ell}\frac{1}{\sum_j g(B_n, I_t + j)}, \text{ for } j \geq -(I_t + \frac{1}{2}) \ . \tag{3.24}$$

Since experimental values of D_ℓ and I_t are commonly available in tables, the level density at the neutron separation energy can be deduced for most nuclei.

A second consideration must also be made before the normalization to $\rho(B_n)$ can be performed. As earlier mentioned, experimental data for γ-ray energies below $E_{\gamma,\min}$ of the γ-ray spectra in the first generation γ-ray matrix has to be omitted, and the experimental level density can then only be extracted up to an energy of $E_f = B_n - E_{\gamma,min}$. This problem is solved by normalizing the extracted level density to an interpolation between the experimental data and the deduced $\rho(B_n)$. The interpolation is calculated by Eq. (3.20), and is normalized to match the deduced $\rho(B_n)$ by a multiplicative factor.

The normalization of the level density at higher excitation energies, is now performed by fitting experimental data points within a selected region at higher excitation energies to the interpolation, and the coefficients A and α are then obtained.

Since α is determined from the normalization of the level density, the only remaining transformation coefficient, B, is determined by the absolute normalization of $\mathcal{T}(E_\gamma)$. This normalization is performed by using experimental values of the average total radiative width $\langle\Gamma_\gamma\rangle$ at the neutron binding energy, and the neutron resonance spacing D_ℓ. The average total radiative width of excited states with energy E_x, spin J and parity π can be described by [21]

$$\begin{aligned}\langle\Gamma_\gamma(E_x,J,\pi)\rangle =& \frac{1}{2\pi\rho(E_x,J,\pi)}\sum_{XL}\sum_{J_f,\pi_f}\int_{E_\gamma=0}^{E_x} dE_\gamma \mathcal{T}_{XL}(E_\gamma) \\ & \times \rho(E_x-E_\gamma,J_f,\pi_f)\ , \end{aligned} \tag{3.25}$$

where X and L denotes the electromagnetic character and multipolarity respectively, and the summation and integration are over all final states with J_f and π_f accessible by γ-transitions of energy E_γ.

It is assumed that the main contribution to the experimental γ-ray transmission coefficient $\mathcal{T}(E_\gamma)$ is of dipole character, i.e. $L=1$. This is because γ-ray transitions of the lowest multipolarity is far more likely to occur than of the higher ones, and the γ-ray transmission coefficient function is then mainly described by

$$B\mathcal{T}(E_\gamma) = B\sum_{XL}\mathcal{T}_{XL}(E_\gamma) \approx B\left[\mathcal{T}_{E1}(E_\gamma)+\mathcal{T}_{M1}(E_\gamma)\right]\ , \tag{3.26}$$

where B is the normalization coefficient. Under the assumption that there is an equal number of accessible states for both parities from any excitation energy and spin, the level density can be expressed as

$$\rho(E_x,J,\pm\pi) = \frac{1}{2}\rho(E_x,J)\ . \tag{3.27}$$

The average total radiative width of neutron capture resonances can be expressed in terms of the experimental γ-ray transmission coefficients as

$$\begin{aligned}\langle\Gamma_\gamma(B_n,I_t+j)\rangle =& \frac{B}{2\pi D_\ell}\int_{E_\gamma=0}^{B_n} dE_\gamma \mathcal{T}(E_\gamma) \\ & \times \rho(B_n-E_\gamma)\sum_{J=-1}^{J=1} g(B_n-E_\gamma,I_t+j+J)\ , \\ & \text{for } j \geq -(I_t+\frac{1}{2})\ , \end{aligned} \tag{3.28}$$

where the spin distribution g of the experimental level density ρ is normalized so that $\sum_J g(E_x,J)\approx 1$, and the limits of J is given by the fact that $L=1$. The experimental value of $\langle\Gamma_\gamma\rangle$ at the neutron binding energy is then a weighted sum

of the level widths of excited states with spin $I_t + j$ for $j \geq -(I_t + \frac{1}{2})$, and the transformation coefficient B can be determined by using the experimental $\langle \Gamma_\gamma(B_n) \rangle$ and D_ℓ available in tables for most nuclei. However, before B can be determined by Eq. (3.28), $\mathcal{T}(E_\gamma)$ is extrapolated with exponential functions at low and high energies due to the omitted data below $E_{\gamma,\min}$, and poor statistics at high E_γ. The extrapolations are performed because the normalization by Eq. (3.28) requires transmission coefficients in the entire energy range of $E_\gamma = 0 - B_n$. The functional form of the fitted extrapolations is

$$\mathcal{T}_{\text{fit}}(E_\gamma) = Ce^{b \cdot E_\gamma} \ , \tag{3.29}$$

where C and b are the fitted parameters. The relation between the γ-ray strength function $f(E_\gamma)$ and the γ-ray transmission coefficients is described by [23]

$$\mathcal{T}_{XL}(E_\gamma) = 2\pi E_\gamma^{2L+1} f_{XL}(E_\gamma) \ . \tag{3.30}$$

Still under the assumption that the main contribution of γ-ray transmissions are of dipole character, the γ-ray strength function is easily calculated by Eq. (3.30)

$$f(E_\gamma) = f_{E1}(E_\gamma) + f_{M1}(E_\gamma) = \frac{1}{2\pi E_\gamma^3} \mathcal{T}(E_\gamma) \ . \tag{3.31}$$

At this point both level densities and γ-ray strength functions have been extracted, and analysis and comparison to models can be performed.

Chapter 4

Results and discussion

Extraction of the level densities, γ-ray transmission coefficients, and γ-ray strength functions from the experimental data will be performed in this chapter.

4.1 Extraction of data

Before extraction of level densities, γ-ray transmission coefficients and subsequently γ-ray strength functions can be performed, the γ-ray energy spectra of the coincidence matrices have to be unfolded, and first generation γ-ray spectra be extracted.

Both unfolding and extraction of first generation γ-ray spectra are performed by the computer program `MaMa` [24], which has the measured response functions of CACTUS embedded in its code. The γ-ray spectra for ^{108}Pd corresponding to excitation energies of $E_x \approx 0.9\,\text{MeV}$ and $6.0\,\text{MeV}$ is shown in Fig. 4.1 for each step of this procedure. One can clearly see the effects on the γ-ray spectra by the unfolding procedure, i.e. the peak structures are refined and their number of counts are increased. The change in the γ-ray spectra after the extraction of first generation γ-rays is also obvious.

A prominent absence of counts can be observed in the first generation γ-ray spectrum corresponding to $E_x \approx 6\,\text{MeV}$ in Fig. 4.1, at about $E_\gamma \approx 1.6\,\text{MeV}$. This arises from a strong decay mode at $E_x = 2046.65\,\text{keV}$ by γ-rays of $E_\gamma = 1612.72$ keV [11], resulting in a large peak structure in the measured γ-ray spectrum at $E_\gamma \approx 1.6\,\text{MeV}$ for excitation energy bins corresponding to $E_x \approx 2\,\text{MeV}$. During the extraction of first generation γ-ray spectra, this prominent peak structure leads to an overestimated subtraction in the γ-ray spectra for higher excitation energies, and is the reason of the methodical problem resulting in the unfortunate $E_{\gamma,\text{min}}$ limit in the subsequent analyses. The extracted first generation γ-ray matrices for ^{107,108}Pd are shown in Fig. 4.2, where the methodical problem at low γ-ray energies

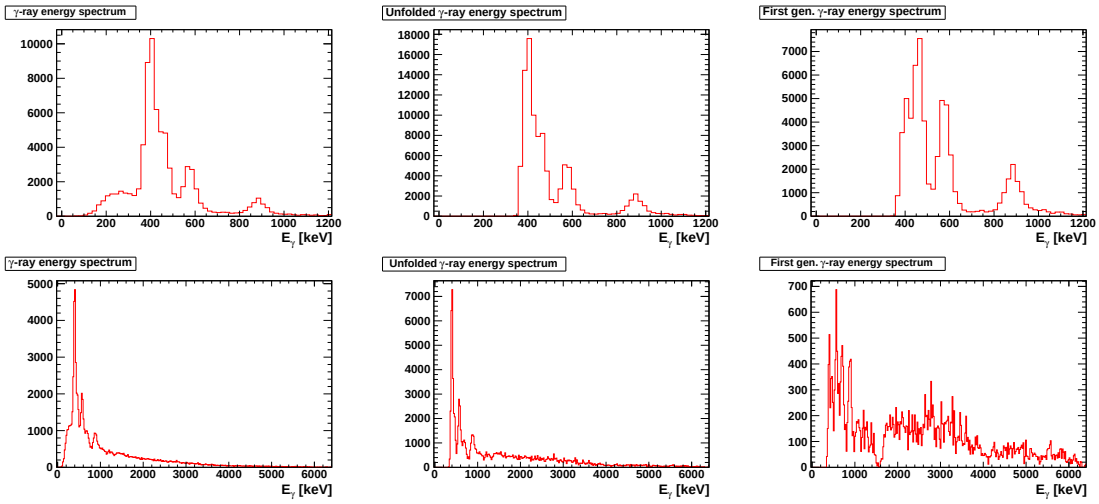

a) Raw spectra. *b) Unfolded spectra.* *c) First generation spectra.*

Figure 4.1: Stepwise change in the γ-ray spectra for ^{108}Pd due to unfolding and extraction first generation γ-ray spectra. The spectra are taken from energies about $E_x \approx 0.9\,\mathrm{MeV}$ (top) and $E_x \approx 6\,\mathrm{MeV}$ (bottom). The number of counts are displayed on the y-axis.

is obvious for both matrices.

The computer code `robin` [25], based on formulas and tables in [19] and [20], is used to obtain various parameters to be used in the analyses. The most relevant parameters are given in Tab. 4.1.

Nucleus	B_n [MeV]	a [MeV^{-1}]	E_1 [MeV]	$\sigma(B_n)$
^{107}Pd	6.536	13.588	−0.625	5.186
^{108}Pd	9.228	13.818	0.789	5.410

Table 4.1: Parameters for the BSFG model, as calculated by robin [25].

Further, the level density at the neutron binding energy is calculated by the program `d2rho` [26], for which input parameters are taken from [31]. The input parameters are given together with the calculated level density in Tab. 4.2. Experimental values for both s- and p-wave neutrons (ℓ=0 and 1 respectively) are used for calculating the level density of ^{107}Pd, and the total level density is then given by

$$\rho_{\mathrm{tot}}(B_n) = \frac{1}{2}\rho_{\ell=0}(B_n) + \frac{1}{2}\rho_{\ell=1}(B_n)\ . \tag{4.1}$$

The experimental first generation γ-ray matrices are used for extraction of level densities and γ-ray transmission coefficients, according to the factorization

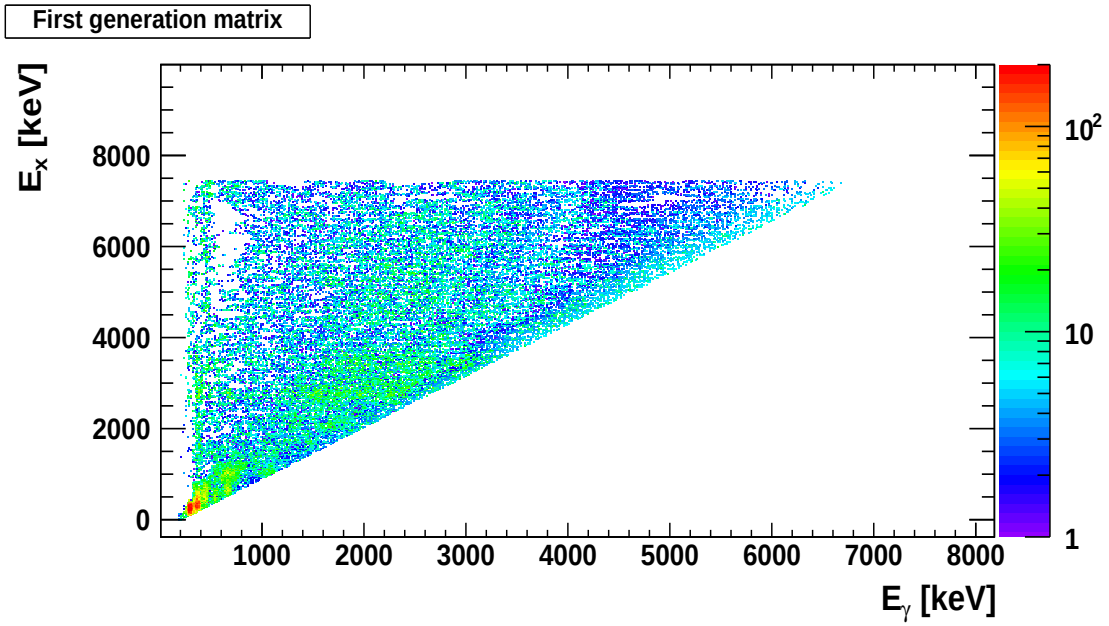

a) ^{107}Pd.

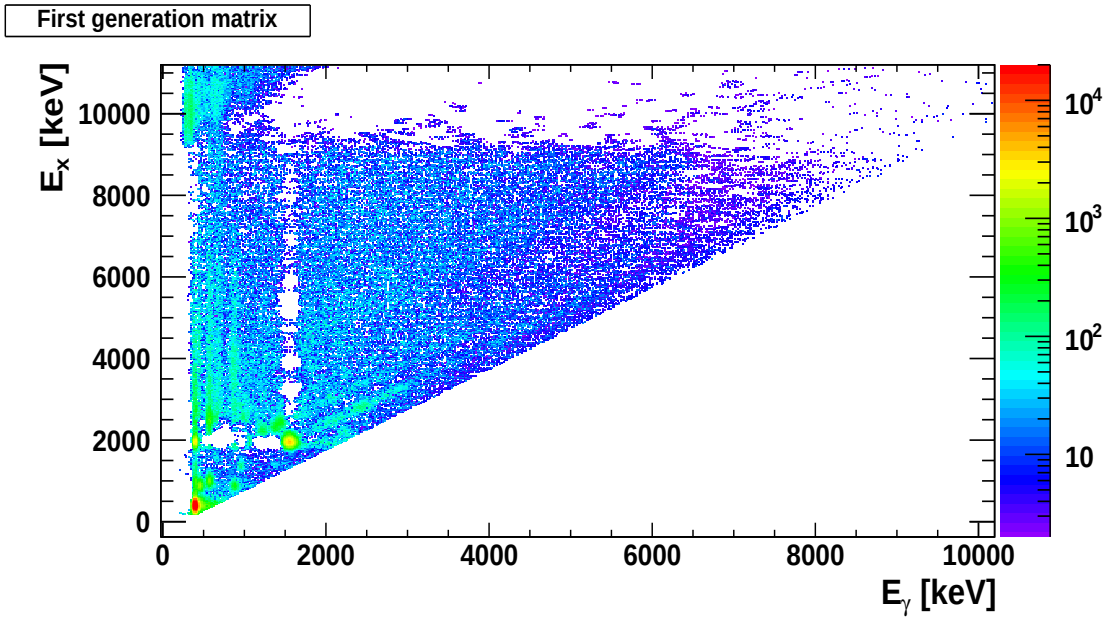

b) ^{108}Pd.

Figure 4.2: The extracted first generation γ-ray matrices of the two nuclei. The number of counts are expressed in colors.

Nucleus	ℓ	I_t	D_ℓ [eV]	σ	$\rho(B_n)$ [MeV^{-1}]
^{107}Pd	0	0	217 ± 60	5.186 ± 0.2593	$2.525 \cdot 10^5 \pm 7.409 \cdot 10^4$
	1	”	85 ± 19	”	$2.230 \cdot 10^5 \pm 5.411 \cdot 10^4$
^{108}Pd	0	5/2	11 ± 0.8	5.410 ± 0.2705	$1.046 \cdot 10^6 \pm 1.159 \cdot 10^5$

Table 4.2: Input parameters for the calculation, and the deduced level density at the neutron binding energy. The total level density for ^{107}Pd *is calculated by Eq. (4.1). The uncertainty of* σ *is taken to be* 5%.

method described in Sec. 3.3. This procedure is performed by the computer code `rhosigchi` [27]. Limits for the extraction are given in Tab. 4.3, and the corresponding areas of the experimental first generation γ-ray matrices are depicted in Figs. 4.3a) and 4.3c). As a consistency check, first generation γ-ray matrices are calculated by the extracted functions according to Eq. (3.16), and the results are shown in Fig. 4.3b) and 4.3d). There seems to be very good agreement between the experimental- and calculated first generation γ-ray matrices, and hence the functions are believed to be successfully extracted. These figures are also nice examples supporting the assumption of factorization stated in relation (3.15).

Nucleus	B_n	$E_{\gamma,\min}$	$E_{x,\min} - E_{x,\max}$	$\rho(E_x)$-interval	$\mathcal{T}(E_\gamma)$-interval
^{107}Pd	6.536	1.0	$2.0 - 6.7$	$0 - 5.7$	$1.0 - 6.7$
^{108}Pd	9.228	1.9	$3.5 - 9.3$	$0 - 7.4$	$1.9 - 9.3$

Table 4.3: Limits for extraction of level densities and γ*-ray transmission coefficients in the first generation* γ*-ray matrices. All energies are given in* MeV. *The last two columns gives the energy range of the two exctracted functions, which are determined by the limits.*

The extracted level densities and γ-ray transmission coefficients are arbitrary solutions, and yet to be normalized to the most physical solutions. Normalization of the level density is performed by the computer code `counting` [28], which also fits exponential functions in the low and high energy regions of the experimental γ-ray transmission coefficients. The normalization of the level density, as well as the extrapolation of the γ-ray transmission coefficients, are displayed in Fig. 4.4. The level densities seem to fit well at low excitation energies, as well as to the interpolations between the experimental data and the deduced level densities at the neutron binding energy. For ^{107}Pd the interpolation fits reasonably well within the uncertainties at data points of the highest excitation energies. The multiplicative factors applied to the interpolations in order to match the deduced level density at the neutron binding energy, are 1.272 and 1.111 for ^{107}Pd and ^{108}Pd respectively. Since these factors are close to unity, the interpolations and the deduced level density seem to be consistent at the neutron binding energy.

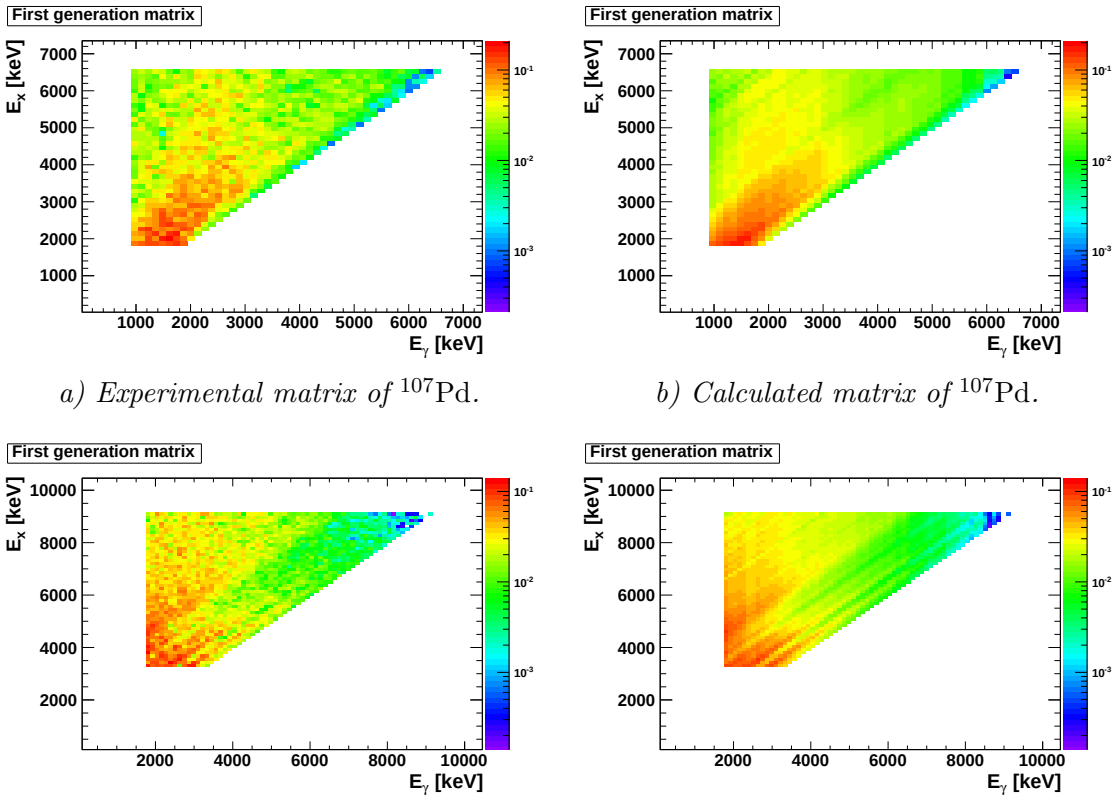

a) Experimental matrix of ^{107}Pd. *b) Calculated matrix of* ^{107}Pd.

c) Experimental matrix of ^{108}Pd. *d) Calculated matrix of* ^{108}Pd.

Figure 4.3: The areas of the experimental first generation γ-ray matrices which are used for extraction, and the corresponding matrices calculated by the extracted functions. The γ-ray spectra are normalized to unity, and the relative γ-decay probabilities for each excitation energy bin are expressed in colors.

The normalized level densities of the two nuclei are depicted for comparison in Fig. 4.5. They are parallel, and the magnitude of the level density of ^{107}Pd is larger. This is due to the unpaired neutron in the even-odd nucleus of ^{107}Pd, where a large number of excited states can be formed by the different spin configurations of this neutron, without first having to overcome the energy to break a nucleon pair. The energy required to break such a pair is about $E \approx 2\,\mathrm{MeV}$, and all the nucleons of the even-even nucleus of ^{108}Pd are paired below this energy. Because of the many possible configurations of an unpaired nucleon below the pair-breaking energy, the total level density is larger for ^{107}Pd. However, ^{108}Pd has a few excited states below the pair-breaking energy as well, which arises from the collective vibrational motion of the nucleons. These few states are responsible for the bumps observed

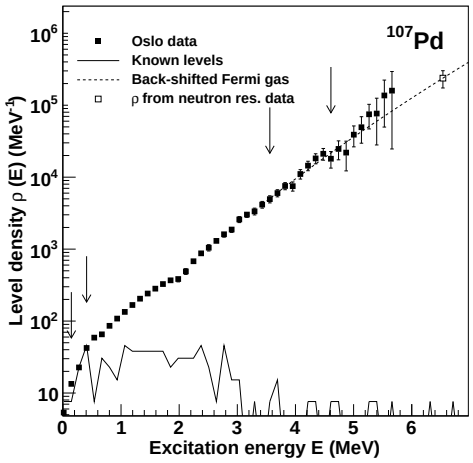

a) $\rho(E_x)$ *of* ^{107}Pd.

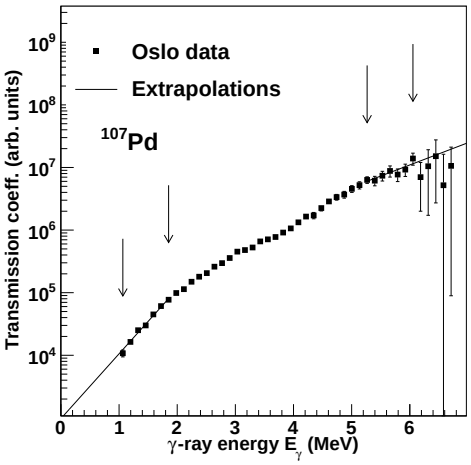

b) $\mathcal{T}(E_\gamma)$ *of* ^{107}Pd.

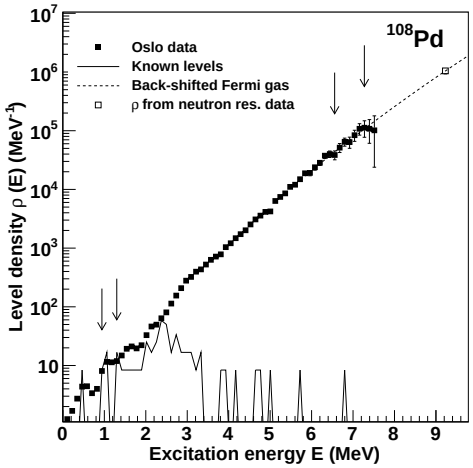

c) $\rho(E_x)$ *of* ^{108}Pd.

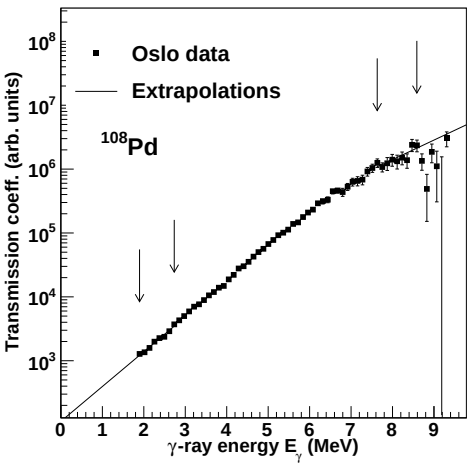

d) $\mathcal{T}(E_\gamma)$ *of* ^{108}Pd.

Figure 4.4: Normalization of the level densities and extrapolation of the γ-ray transmission coefficients for the two nuclei. The fits are performed between the arrows, which denote the fit limits.

below $E_x \approx 2\,\text{MeV}$ in the level density of ^{108}Pd. Before explanation of these states, it should be stated that the nuclear vibrational motion is quantified by quadrupole phonons. The first bump comes from the first vibrational 2^+ excited state at $E_x = 433.94\,\text{keV}$ [11], originating from one quadrupole phonon. The second bump comes from the 0^+, 2^+, and 4^+ triplet at $E_x = 1052.8\,\text{keV}$, 931.15

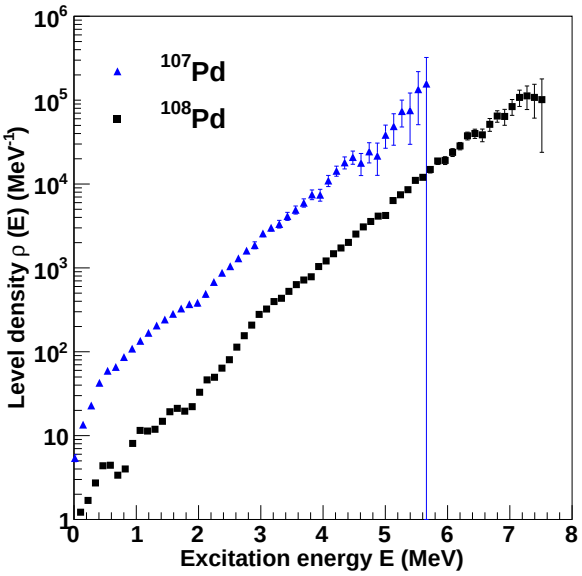

Figure 4.5: Comparison of the normalized level densities of the two nuclei.

keV, and 1048.2 keV respectively [11]. These states are formed by two quadrupole phonons, and are at about twice the energy as the first vibrational state. The third bump at $E_x \approx 1.5$ MeV probably comes from three quadrupole phonons, and above $E_x \approx 2$ MeV pair-breaking comes into play. This is also observable in the level density of ^{107}Pd, and above the pair-breaking energy the level densities of ^{107}Pd and ^{108}Pd are more or less parallel. To demonstrate the significant difference between even-odd and even-even nuclei because of the nucleon pairing, it can be mentioned that ^{107}Pd has 57, and ^{108}Pd has 12 known excited states below $E_x \approx 2$ MeV.

The slope α of Eqs. (3.18) and (3.19) for both functions is determined in the normalization of the level density, and the only remaining normalization coefficient to be determined is the absolute normalization B of the γ-ray transmission coefficients. This is performed by the program `normalization` [29], which simultaneously calculates the γ-ray strength functions corresponding to Eq. (3.30). The input parameters used for the normalization is given in Tab. 4.4.

Nucleus	ℓ	I_t	D_ℓ [eV]	$\langle\Gamma_\gamma\rangle$ [MeV]
^{107}Pd	1	0	85	102
^{108}Pd	0	5/2	11	125

Table 4.4: Parameters used in the normalization of the γ-ray transmission coefficients. They were taken from [31].

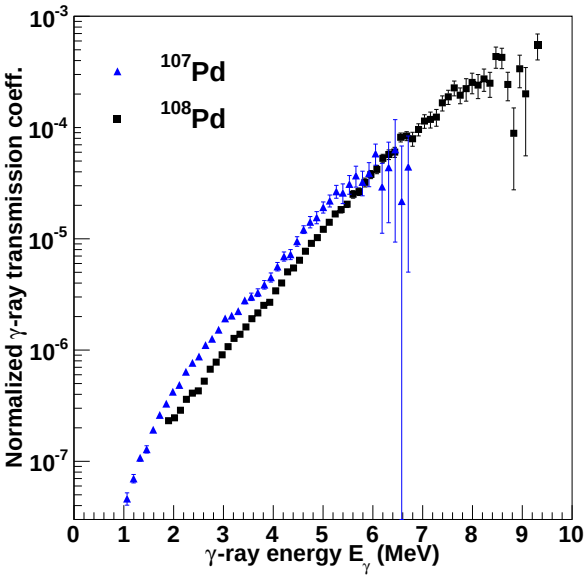

Figure 4.6: Comparison of the normalized γ-ray transmission coefficients for the two nuclei.

The normalized γ-ray transmission coefficients for the two nuclei are depicted in Fig. 4.6, where it can be observed that the γ-ray transmission coefficients for ^{107}Pd have a bit higher magnitude than the corresponding ones for ^{108}Pd. This might come from the extrapolation in the lower γ-ray energy region, where the data of ^{107}Pd bends downwards for $E_\gamma < 2\,\text{MeV}$ resulting in a steeper slope in the extrapolation than for ^{108}Pd. The same characteristics for $E_\gamma < 2\,\text{MeV}$ may actually also be the case for ^{108}Pd, since neighbouring nuclei tends to be similar. Unfortunately, this cannot be investigated because of the lower limit of $E_{\gamma,\text{min}} = 1.9$ MeV for ^{108}Pd. Overall, the two sets of γ-ray transmission coefficients are very similar, and in the end it is the shape of the γ-ray strength function that is of main interest.

The calculated γ-ray strength functions are depicted in Fig. 4.7. Generally, the γ-ray strength functions are expected to be similar for neighbouring nuclei, which they are in this case for energies $E_\gamma > 4\,\text{MeV}$. However, below this energy the γ-ray strength functions deviate unexpectedly. In the case of ^{107}Pd, it seems to be more enhanced with respect to the one of ^{108}Pd, which might be due to a resonance below $E_\gamma \approx 4\,\text{MeV}$. In contrast, the case seems to be quite opposite for ^{108}Pd, as the γ-ray strength function descends more rapidly, then flattens out and possibly starts to rise. This last observation might as well be an optical illusion, created by the two data points at $E_\gamma \approx 2.5\,\text{MeV}$ and the data point at $E_{\gamma,\text{min}}$.

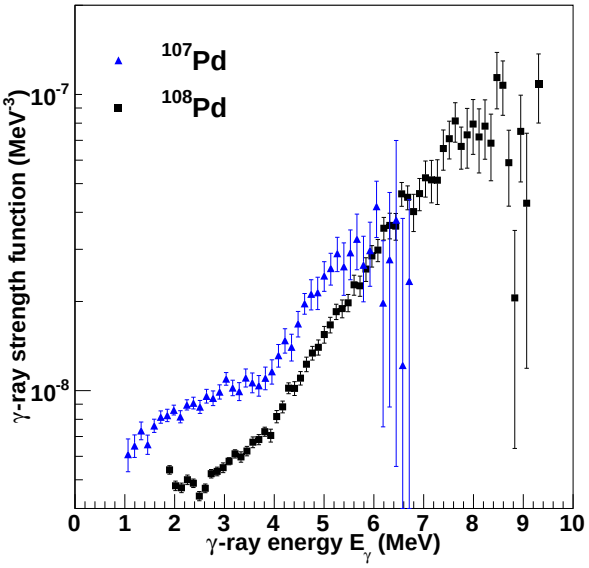

Figure 4.7: Comparison of the γ-ray strength functions of the two nuclei.

The extracted strength functions deviates much for $E_\gamma < 4\,\text{MeV}$, which is unexpected. A possible explanation worth investigation, is if the experimental data at lower excitation energies has dominated in the fitting procedure due to the relative greater number of counts. Therefore, new lower limits of excitation energy are placed in the first generation γ-ray matrices, in order to investigate the importance of these on the extracted functions. By observing the normalized experimental first generation γ-ray matrices in Fig. 4.3, the new lower limits are determined to $E_{x,\text{min}} = 3.5\,\text{MeV}$ and $5.2\,\text{MeV}$ for ^{107}Pd and ^{108}Pd respectively. Note that these limits are deliberately overestimated, in order to make potential differences more obvious. The extraction procedure is performed in the same way as before, and extracted data by the new limits are compared to the originally extracted data in Fig. 4.8.

The correspondence between the extracted functions of the new and old limits are so good, that the deviation in the γ-ray strength functions for $E_\gamma < 4\,\text{MeV}$ does not seem to arise from unfortunately placed limits for the extraction procedure. However, there is a slight difference in the level density of ^{108}Pd at energies below $E_x \approx 1\,\text{MeV}$. This seems to be due to the relatively high count rates observed for the γ-decay to $E_x = 433.94\,\text{keV}$ in the excitation energy region from $E_x = 2046.65$ keV to energies just above $E_x \approx 3.5\,\text{MeV}$, as seen in Fig. 4.2b). In light of these observations, final lower limits on the excitation energy in the first generation γ-ray matrices are decided to be $E_{x,\text{min}} = 2.8\,\text{MeV}$ and $4.0\,\text{MeV}$ for ^{107}Pd and

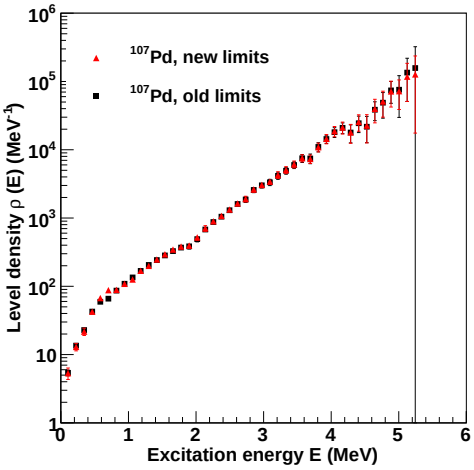

a) Normalized $\rho(E_x)$ for ^{107}Pd.

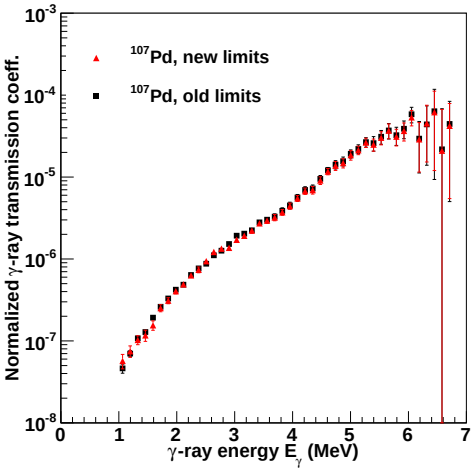

b) Normalized $\mathcal{T}(E_\gamma)$ for ^{107}Pd.

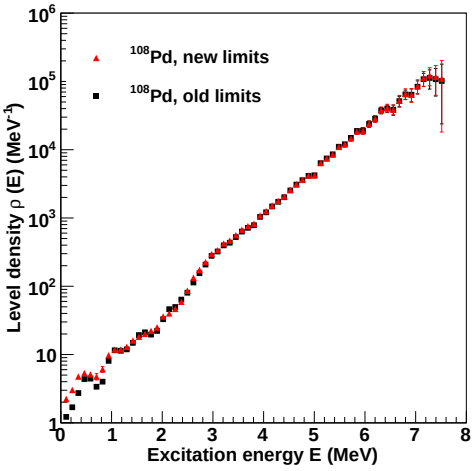

c) Normalized $\rho(E_x)$ for ^{108}Pd.

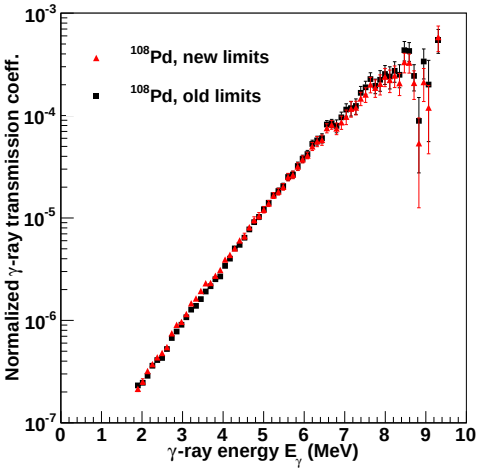

d) Normalized $\mathcal{T}(E_\gamma)$ for ^{108}Pd.

Figure 4.8: Comparison between the extracted data of new and old limits in E_x.

^{108}Pd respectively. The final limits are chosen as a compromise between the new and old limits just investigated, in order to avoid the highest relative count rates and simultanously take advantage of most of the experimental data. The final extracted level densities and γ-ray strength functions are shown in Fig. 4.9, and are the ones to be used in the further analyses. The corrresponding normalized first generation γ-ray matrices are depicted in Fig. 4.10 to show the consistency of the new extracted functions, which seems to be very good.

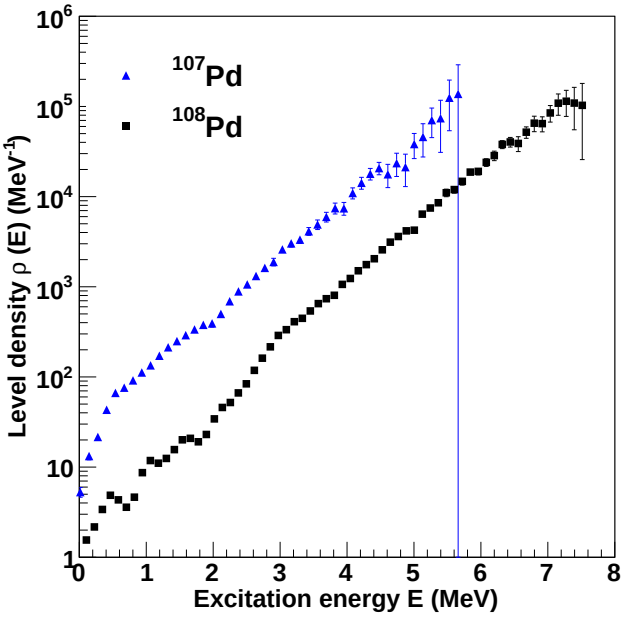

a) Compared level densities.

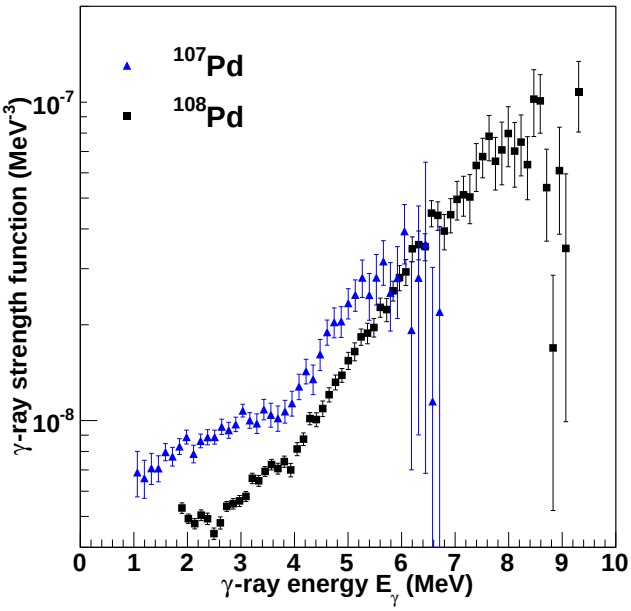

b) Compared strength functions.

Figure 4.9: The final extracted level densities and γ-ray strength functions.

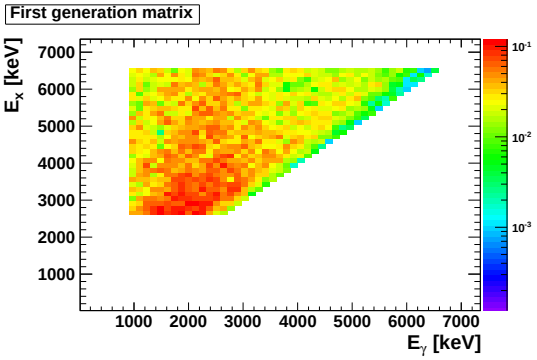

a) Experimental matrix of ^{107}Pd.

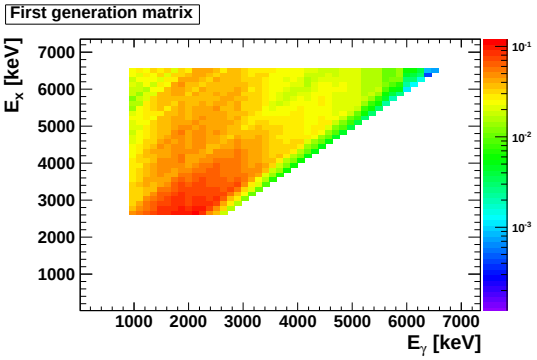

b) Calculated matrix of ^{107}Pd.

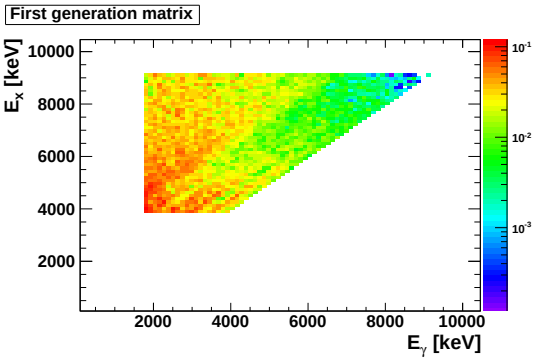

c) Experimental matrix of ^{108}Pd.

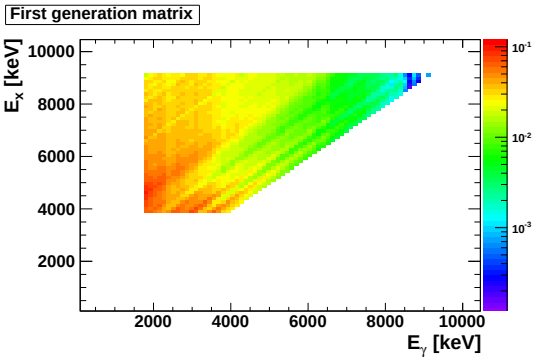

d) Calculated matrix of ^{108}Pd.

Figure 4.10: The areas of the experimental first generation γ-ray matrices which are used for extraction, and the corresponding matrices calculated by the extracted functions. The γ-ray spectra are normalized to unity, and the relative γ-decay probabilities for each excitation energy bin are expressed in colors.

4.2 Observations in the level densities

Before proceeding to the more extensive investigation of the γ-ray strength functions, it is appropriate to first summarize the findings for the level densities of ^{107,108}Pd.

Structures, probably due to excited states formed by 1, 2 and 3 quadrupole phonons are observed in the level density of ^{108}Pd. In the level density of ^{107}Pd, these structures are smeared out and disappear among the high number of available states for the valence neutron. Both level densities for ^{107,108}Pd exhibit a sudden increase in magnitude at about $E_x \approx 2\,\text{MeV}$, which is probably due to the breaking of nucleon pairs. For energies above $E_x \approx 3\,\text{MeV}$, the level densities exhibit the same constant increase in magnitude, and are parallel. In this region, the characteristics can be described by the constant temperature formula [19]

$$\rho(E_x) = \frac{1}{T} e^{(E_x - E_0)/T} \ , \tag{4.2}$$

where T is the temperature, E_x is the excitation energy and E_0 is the energy backshift. Both T and E_0 are fit parameters in this model. A rough estimation of the temperature is performed by determining the slope of the increase in the level densities in this region, and the estimated values are provided in Tab. 4.5.

Nucleus	$E_{x,1}$ [MeV]	$E_{x,2}$ [MeV]	T [MeV]
^{107}Pd	3.0	4.6	0.67
^{108}Pd	3.1	6.4	0.68

Table 4.5: Estimated temperature from the slope of the level densities. Columns 2 and 3 indicate the position of the points used in the determination of the slope, and the level densities used for the estimation are the ones depicted in Fig. 4.9a).

The entropy difference of the nuclei due to the valence neutron can be described by

$$\Delta S = \ln\left(\frac{\rho_{107}(E_x)}{\rho_{108}(E_x)}\right) k_B \ , \tag{4.3}$$

where k_B is the Boltzmann constant. The magnitude of the level density of ^{107}Pd is approximately 7.8 times larger than for ^{108}Pd at $E_x > 3\,\text{MeV}$, and this yields $\Delta S \approx \ln(7.8) = 2.06 k_B$.

Since this work is mainly focused on the investigation of the γ-ray strength functions, the level density results will not be elaborated further.

4.3 Comparison to resonance models

The extracted experimental γ-ray strength functions for the two nuclei are in this section to be compared to resonance models. First, the systematics of the most important models will be introduced.

4.3.1 The GEDR and GMDR models

The largest and most important resonances are the GEDR[1] and GMDR[2], which for systematic models have been developed. The models to be used in this investigation, are the standard- and enhanced generalized Lorentzian models for the electric dipole resonance $E1$, and the spin-flip resonance model for the magnetic dipole resonance $M1$. In the standard Lorentzian model, the $E1$ strength function has a Lorentzian shape with an energy independent width, and is described by [23]

$$f_{E1}^{SLO}(E_\gamma) = c \cdot \frac{\sigma_r E_\gamma \Gamma_r^2}{(E_\gamma^2 - E_r^2)^2 + E_\gamma^2 \Gamma_r^2} \ , \tag{4.4}$$

where σ_r, E_r, and Γ_r is the peak cross section, energy centroid, and width of the resonance respectively. The factor $c = (3\pi^2\hbar^2c^2)^{-1} = 8.674 \cdot 10^{-8}\,\mathrm{mb^{-1}MeV^{-2}}$ [23] gives the conversion of the Lorentzian to units of MeV^{-3}.

The enhanced generalized Lorentzian model on the other hand, takes into account that the width of the $E1$ resonance is energy E_γ and temperature T dependent, and includes in addition a term corresponding the strength function at $E_\gamma = 0$. The enhanced generalized Lorentzian is described by [23]

$$f_{E1}^{EGLO}(E_\gamma) = c \cdot \sigma_r \Gamma_r \left[\frac{E_\gamma \Gamma_{E_n}(E_\gamma, T)}{(E_\gamma^2 - E_r^2)^2 + E_\gamma^2 \Gamma_{E_n}^2(E_\gamma, T)} + 0.7 \cdot \frac{\Gamma_{E_n}(0,T)}{E_r^3} \right] \ , \tag{4.5}$$

where

$$\Gamma_{E_n}(E_\gamma, T) = \left[k_0 + (1 - k_0) \frac{(E_\gamma - \epsilon_0)}{E_r - \epsilon_0} \right] \Gamma_K(E_\gamma, T) \ , \tag{4.6a}$$

$$\Gamma_K(E_\gamma, T) = \frac{\Gamma_r}{E_r^2}(E_\gamma^2 + 4\pi^2 T^2) \ . \tag{4.6b}$$

The enhancement factor k_0 is used to reproduce the experimental $E1$ strength around the reference energy $\epsilon_0 = 4.5\,\mathrm{MeV}$, and for the BSFG model this factor can be written as

$$k_0 = \begin{cases} 1 & \text{for } A < 148 \\ 1 + 0.09(A - 148)^2 e^{-0.18(A-148)} & \text{for } A \geq 148 \ , \end{cases} \tag{4.7}$$

[1] Giant electric dipole resonance
[2] Giant magnetic dipole resonance

where A is the mass number of the nucleus. For the nuclei in this experiment, $k_0 = 1$, and the enhanced generalized Lorentzian model is reduced to the generalized Lorentzian model, where $\Gamma_{E_n}(E_\gamma, T) = \Gamma_K(E_\gamma, T)$.

If experimental GEDR parameters are lacking, which is the case for ^{107,108}Pd, systematic parameters are used in the calculation of Eqs. (4.4) and (4.5). The systematics are reliable for nuclei with $A > 40$, in the vincinity of the β-stability line. They are given in [23] and will be explained in the following.

Global parameterization of spherical nuclei is given by

$$\begin{aligned} E_r &= 31.2A^{-\frac{1}{3}} + 20.6A^{-\frac{1}{6}}\,\text{MeV}\ , \\ \Gamma_r &= 0.026E_r^{1.91}\,\text{MeV}\ , \\ \sigma_r &= 1.2 \cdot \frac{120NZ}{A\pi\Gamma_r}\,\text{mb}\ , \end{aligned} \tag{4.8}$$

where N and Z is the number of neutrons and protons respectively. Further, the global parameterization of deformed nuclei is given by

$$\begin{aligned} E_{r,1} &= \frac{E_{r,2}}{0.911(a_0/b_0) + 0.089}\ , & E_{r,2} &= \frac{E_r}{b_0}\left[1 - 1.151 \cdot 10^{-2}(a_0^2 - b_0^2)\right]\ , \\ \Gamma_{r,1} &= 0.026E_{r,1}^{1.91}\ , & \Gamma_{r,2} &= 0.026E_{r,2}^{1.91}\ , \\ \sigma_{r,1} &= \frac{2\sigma_r}{3}\ , & \sigma_{r,2} &= \frac{\sigma_r}{3}\ , \end{aligned} \tag{4.9}$$

where index 1 and 2 represent the axis along and perpendicular to the axis of symmetry respectively. The variables a_0, b_0 are found by the relations

$$a_0 = \frac{1 + \alpha_2}{\lambda}\ , \tag{4.10a}$$

$$b_0 = \frac{1 - 0.5\alpha_2}{\lambda}\ , \tag{4.10b}$$

$$\alpha_2 = \beta_2\left(\frac{5}{4\pi}\right)^{\frac{1}{2}}\ , \tag{4.10c}$$

$$\lambda = \left(1 + \frac{3}{5}\alpha_2^2 + \frac{2}{35}\alpha_2^3\right)^{\frac{1}{3}}\ , \tag{4.10d}$$

where β_2 is the quadrupole deformation parameter.

The M1 spin-flip resonance is described by Eq. (4.4), with its own specific parameters. The systematic GMDR parameters are given by

$$\begin{aligned} E_r &= 41A^{-\frac{1}{3}}\,\text{MeV}\ , \\ \Gamma_r &= 4\,\text{MeV}\ , \\ \sigma_r &= \text{adjusted to:} \\ &\qquad f_{E1}/f_{M1} = 0.0588A^{0.878} \text{ at } E_\gamma = 7\,\text{MeV}\ . \end{aligned} \tag{4.11}$$

4.3.2 Description of the γ-ray strength functions

In order to describe the characteristics of the extracted γ-ray strength functions, comparison to models and adjustment of corresponding fit parameters will be performed. The parameters β_2 and T are needed in the systematic model calculations, and the values are listed in Tab. 4.6. The ground state deformation parameters are theoretically derived from the HFB ground-state prediction [23], and the values are found in the corresponding HFB-2 mass table. The temperatures T is taken from constant temperature fits to discrete levels [23], which are found in tables at [31].

Nucleus	β_2	T [MeV]
^{107}Pd	0.2	0.51452
^{108}Pd	0.2	0.51006

Table 4.6: The ground state deformation parameters and the temperatures used in the calculation of the systematic parameters.

Systematic GEDR and GMDR parameters were then calculated, and are listed in Tabs. 4.7 and 4.8.

Nucleus	E_{r1} [MeV]	Γ_{r1} [MeV]	σ_{r1} [mb]	E_{r2}	Γ_{r2} [MeV]	σ_{r2} [mb]
^{107}Pd	14.41	4.25	154.11	17.06	5.86	76.94
^{108}Pd	14.38	4.23	155.84	17.02	5.84	77.80

Table 4.7: Systematic GEDR parameters.

Nucleus	E_r [MeV]	Γ_r [MeV]	σ_r [mb]
^{107}Pd	8.64	4.0	0.94
^{108}Pd	8.61	4.0	0.95

Table 4.8: Systematic GMDR parameters.

Comparisons of the extracted γ-ray strength functions and giant dipole resonance models for the two nuclei are shown in Fig. 4.11. The γ-ray strength function of ^{108}Pd is also compared to experimental data from (γ, n) measurements [32], for which the numbers are found in tabulated form at [33]. The models have been calculated using systematic parameters, which might be adjusted within reasonable limits to possibly acheive better agreement between the models and experimental data.

The standard Lorentzian model overestimates the experimental data at all energies covered by the Oslo data, and the total γ-ray strength function is thus in

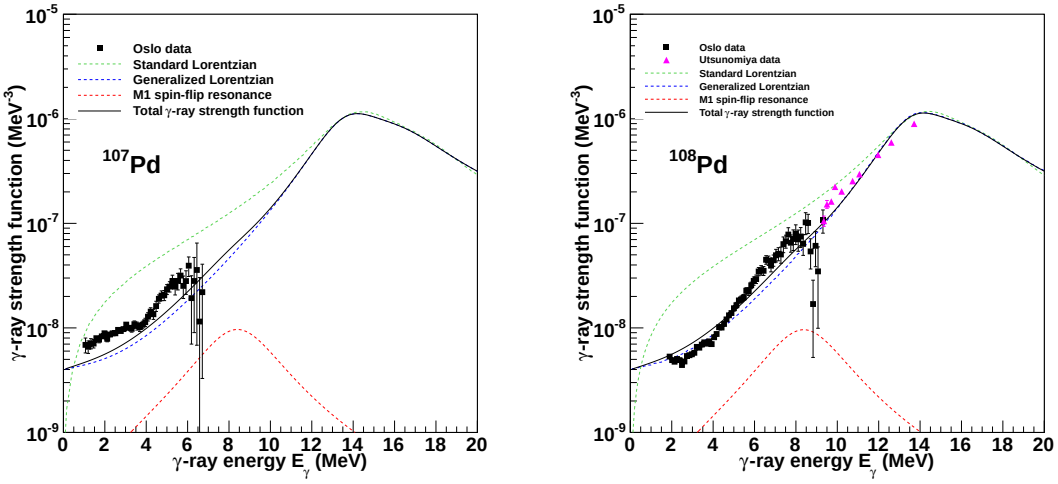

a) ^{107}Pd *b)* ^{108}Pd

Figure 4.11: The γ-ray strength functions compared to models with systematic parameters. The total γ-ray strength function is composed of f_{E1} of the enhanced generalized Lorentzian and f_{M1} of the spin-flip model.

the first round taken to be described by

$$f_{\text{tot}} = f_{E1}^{EGLO} + f_{M1} \ . \tag{4.12}$$

Despite the difference in the γ-ray strength functions as mentioned earlier, the experimental data of the two nuclei seem to agree of an enhancement in the γ-ray strength for $E_\gamma > 4\,\text{MeV}$, which is also supported by Utsunomiya data for ^{108}Pd. To explain the characteristics of the experimental γ-ray strength functions as compared to the models, a series of speculations will be discussed in the following.

First, the total γ-ray strength function is to be described by the models as

$$f_{\text{tot}} = k \cdot (f_{E1}^{EGLO} + f_{M1}) \ , \tag{4.13}$$

where k is a normalization constant used to adjust the magnitude of the model prediction to match the experimental one.

Further, the γ-ray strength enhancement at lower γ-ray energies found for iron and molybdenum has previously been described as [2]

$$f_{\text{upb}} = c \cdot A E_\gamma^{-b} \ , \tag{4.14}$$

where A and b are fit parameters, and c is the conversion factor defined in the beginning of the section. The pygmy resonance observed for tin has been described

as [5]

$$f_{\text{pyg}} = C_{\text{pyg}} \frac{1}{\sqrt{2\pi}\sigma_{\text{pyg}}} e^{-(E_\gamma - E_{\text{pyg}})^2/2\sigma_{\text{pyg}}^2} \ , \tag{4.15}$$

where C_{pyg}, σ_{pyg} and E_{pyg} is the normalization constant, standard deviation, and energy centroid of the resonance respectively.

With these model considerations in place, fits to the experimental data can be performed in order to investigate the characteristics of the γ-ray strength functions more closely. In the case of ^{107}Pd, as shown in Fig. 4.11a), the model prediction and the Oslo data fits roughly only at about $E_\gamma \approx 4\,\text{MeV}$. For energies above this, the experimental data exhibits a slight enhancement as compared to the model. Below $E_\gamma \approx 4\,\text{MeV}$, enhancement as compared to the model is observed as well. This might indicate a resonance between $E_\gamma = 2 - 4\,\text{MeV}$, and might also be temperature related. It should also be noted that the error bars at the points of lowest energy are such that it is difficult to determine whether the γ-ray strength continues to descend or if it flattens out for lower E_γ. However, the enhancements in the γ-ray strength of the experimental data between $E_\gamma = 2 - 4$ MeV and for $E_\gamma > 4\,\text{MeV}$ are obvious. The first approach to match the model prediction to experimental data, was to adjust the temperature T in the calculation of the enhanced generalized Lorentzian. It was set to $T = 0.7\,\text{MeV}$, which is a reasonable value since it was approximately estimated by the slope of the level density. The normalization constant was adjusted to $k = 0.8$, and as depicted in Fig. 4.12a), this results in nice correspondence between experimental data and model for $E_\gamma < 4\,\text{MeV}$. Subsequently, a pygmy resonance is added in order to investigate the enhancement in the experimental data for $E_\gamma > 4\,\text{MeV}$, and the result is depicted in Fig. 4.12b). The initial parameters for the pygmy resonance was taken to be the same as for tin [5], and the resulting model description seems to fit the experimental data nicely without significant adjustment of the parameters. This supports the presence of a pygmy resonance for ^{107}Pd, and the parameters are listed in Tab. 4.9. In the latter approach, depicted in Fig. 4.12b), the total γ-ray strength function is described by

$$f_{\text{tot}} = k \cdot (f_{E1}^{EGLO} + f_{M1} + f_{\text{pyg}}) \ , \tag{4.16}$$

which reproduce the experimental data pretty well.

k	T [MeV]	C_{pyg} [MeV^{-2}]	σ_{pyg} [MeV]	E_{pyg} [MeV]
0.8	0.7	$3.2 \cdot 10^{-7}$	1.4	8.1

Table 4.9: Parameters used in the fit of the model to the experimental data, shown in Fig. 4.12. The parameters for the pygmy resonance are strikingly similar to those of Sn *[5].*

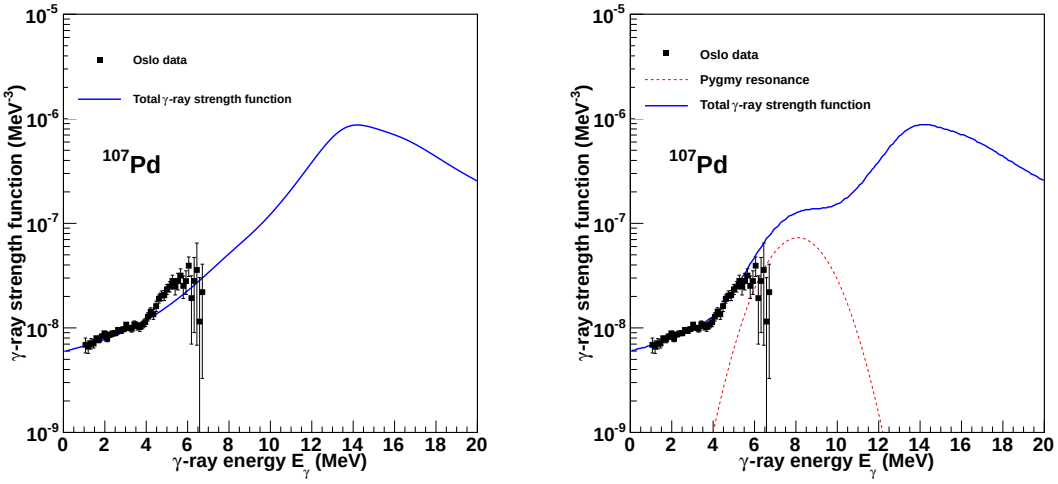

a) Model prediction with the temperature adjusted.

b) Model prediction with the temperature adjusted and pygmy resonance included.

Figure 4.12: The investigation of temperature related effects in ^{107}Pd. *A pygmy resonance is also added to investigate the enhancement above* $\approx$ *4 MeV.*

Note that the model has only been visually fitted since this is done of speculative reasons, and there has not been any attempts to obtain the exact parameters. This goes for all the following fits as well.

The enhancement at energies below $E_\gamma \approx 4\,\mathrm{MeV}$ might also be due to a low lying resonance, which will now be investigated. This resonance is assumed to be described by Eq. (4.15), and the temperature is reset to the initial value given in Tab. 4.6. The total γ-ray strength function is then described by

$$f_{\mathrm{tot}} = k \cdot (f_{E1}^{EGLO} + f_{M1} + f_{\mathrm{pyg}} + f_{\mathrm{pyg2}}) \,, \tag{4.17}$$

where f_{pyg2} is the speculative resonance for $E_\gamma < 4\,\mathrm{MeV}$. This approach also seems to reproduce the experimental data very nicely, and is in addition more consistent with the temperature of the constant temperature fits. The bow shape in the γ-ray strength function for $E_\gamma < 4\,\mathrm{MeV}$ seems to be reproduced better with this approach as well. Note that the parameters of the pygmy resonance at $E_\gamma > 4$ MeV was also slightly adjusted in this approach, as compared to the first approach when the temperature was adjusted. However, the adjusted parameters do not differ significantly, as can be seen in Tab. 4.10.

In the case of ^{108}Pd, the model prediction of the total γ-ray strength function seems to overestimate the experimental values both for Oslo data at $E_\gamma < 4$ MeV, and Utsunomiya data at the highest data points. This can be observed

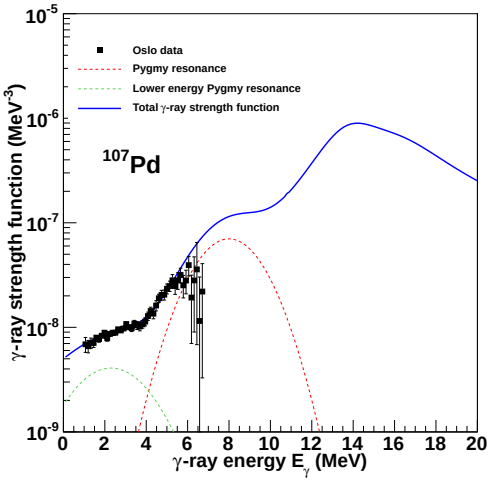

Figure 4.13: Investigation of the possibility of a lower energy resonance in the γ-ray strength function of ^{107}Pd.

k	C_{pyg} [MeV^{-2}]	σ_{pyg} [MeV]	E_{pyg} [MeV]
0.8	$3.3 \cdot 10^{-7}$	1.5	8.0
k	C_{pyg2} [MeV^{-2}]	σ_{pyg2} [MeV]	E_{pyg2} [MeV]
0.8	$2.3 \cdot 10^{-8}$	1.8	2.3

Table 4.10: The parameters used in the fit to the experimental data, shown in Fig. 4.13.

in Fig. 4.11b). To correct for this overestimation, the normalization constant of Eq. (4.13) is set to $k = 0.8$ in consistency with the value found for ^{107}Pd. As can be seen in Fig. 4.14, the model now fits both the mentioned data regions much better. Between $E_\gamma \approx 4 - 12\,\mathrm{MeV}$, a slight enhancement of the experimental data as compared to the model is observed. Both the experimental data sets plotted in Fig. 4.14 agree on this fact, and this enhancement indicates the presence of a pygmy resonance for ^{108}Pd, which is also consistent with the observations for ^{107}Pd. At energies below $E_\gamma \approx 4\,\mathrm{MeV}$, the experimental data and the model agree well, except for a small uprise in the experimental data at $E_\gamma \approx 2\,\mathrm{MeV}$. This is only indicated by a few data points, and the appearance may also be enhanced by an illusion created by the lowest data points as described earlier. In order to investigate the enhancement above $E_\gamma \approx 4\,\mathrm{MeV}$, a pygmy resonance is fitted according to Eq. (4.16), and the corresponding fit parameters are found in Tab. 4.11. Due to the uprise in the γ-ray strength function at $E_\gamma \approx 2\,\mathrm{MeV}$, a softpole resonance is also added to investigate a possible upbend at lower energies. As mentioned the signs of upbend are very weak, and it is also contradicted by the data of ^{107}Pd. In addition, the value of b is really high compared to data in [3], and all these observations argue against the possible existence of an upbend

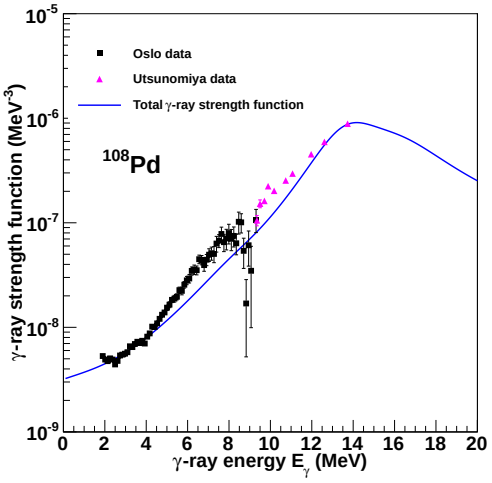

Figure 4.14: The total γ-ray strength function model for ^{108}Pd has been adjusted to fit the experimental data better.

in the γ-ray strength function of ^{108}Pd. However, with the upbend included, the total γ-ray strength function is described by

$$f_{\text{tot}} = k \cdot (f_{E1}^{EGLO} + f_{M1} + f_{\text{pyg}} + f_{\text{upb}}) \; . \tag{4.18}$$

The fits of the γ-ray strength function of ^{108}Pd are depicted in Fig. 4.15. At least the pygmy resonance for $E_\gamma > 4\,\text{MeV}$ seems to be strongly supported by the experimental data sets of both nuclei, but note the difference in E_{pyg}.

k	C_{pyg} [MeV^{-2}]	σ_{pyg} [MeV]	E_{pyg} [MeV]	A [mb/MeV]	b
0.8	$3.5 \cdot 10^{-7}$	1.7	9.3	0.24	4.8

Table 4.11: Parameters of the pygmy- and softpole resonances included in the model description of the total γ-ray strength function of ^{108}Pd.

A possible explanation for this might be the absolute normalization of the transmission coefficients. The characteristics of the γ-ray strength functions of the two nuclei above $E_\gamma \approx 4\,\text{MeV}$ are essentially identical, except for the difference in magnitude.

As a last, very speculative investigation, the strength functions will be normalized to eachother. This is tested because of the mentioned difference in extrapolations at low E_γ in the transmission coefficients, and because of the relative large deviation in the magnitudes of the γ-ray strength functions. The normalization coefficient for achieving this will be determined by the relative values of the magnitudes of the γ-ray transmission coefficients of ^{108}Pd and ^{107}Pd, which are shown in Fig. 4.16. The relative values of the γ-ray transmission coefficients are averaged in the energy region where they are parallel, i.e. between $E_\gamma = 3.5 - 5.3\,\text{MeV}$, and

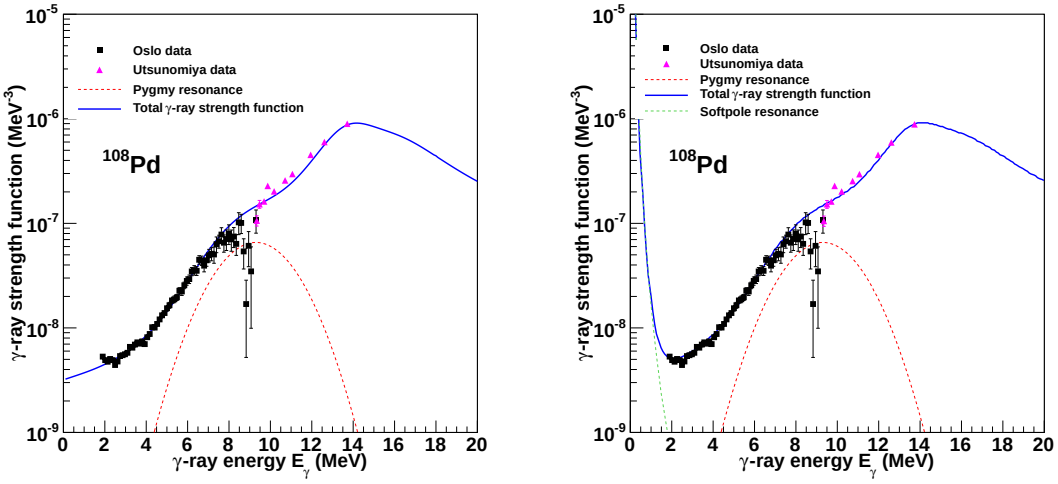

a) Inclusion of pygmy resonance *b) Inclusion softpole resonance*

Figure 4.15: Pygmy- and softpole resonances are included to investigate the characteristics of the γ-ray strength function.

the values are also weighted with respect to the relative number of data points. This energy region is also where the γ-ray strength functions are parallel. The average relative value is found to be $\mathcal{T}(^{108}\mathrm{Pd})/\mathcal{T}(^{107}\mathrm{Pd}) = 0.65$, and is used to normalize the γ-ray strength functions to eachother, i.e. by multiplication in the case of ^{107}Pd and by division in the case of ^{108}Pd.

The re-normalized γ-ray strength functions are depicted in Fig. 4.17, which shows that the normalization constant is nicely determined. Even the large discrepancy for $E_\gamma < 4\,\mathrm{MeV}$ is almost gone.

In the case of ^{108}Pd, the re-normalized γ-ray strength function is compared to models and Utsunomiya data, and a satisfying observation is that it still fits the Utsunomiya data very well. Here, the total γ-ray strength function is described by Eq. (4.16), and the temperature has been adjusted in order for the model to fit data at $E_\gamma < 4\,\mathrm{MeV}$. The parameters of this model reproduction of the total γ-ray strength function, are listed in Tab. 4.12. As can be seen, the parameters of the pygmy resonance, as well as the adjusted temperature, are very similar to the corresponding ones obtained for ^{107}Pd in Tab. 4.9.

k	C_{pyg} [MeV^{-2}]	σ_{pyg} [MeV]	E_{pyg} [MeV]	T
0.8	$3.5 \cdot 10^{-7}$	1.5	8.3	0.66

Table 4.12: Speculative ^{108}Pd pygmy resonance parameters. T was also adjusted.

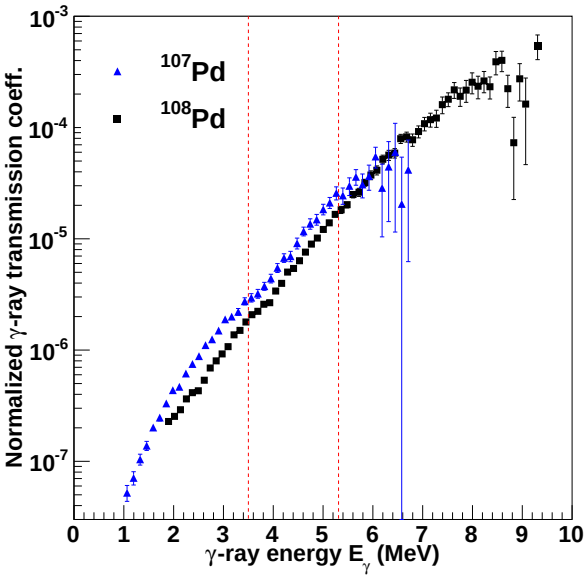

Figure 4.16: Normalized transmission coefficients. The red dotted lines indicate the region where the relative values are averaged.

As for the case of ^{107}Pd, the total γ-ray strength function is compared to the model description of Eq. (4.17), with the parameters listed in Tab. 4.13. The parameters of the pygmy resonance are now comparable to the ones for ^{108}Pd in Tab. 4.11, and the temperature is the one given by the constant temperature fit. However, the model reproduction seems to overestimate the experimental values slightly about $E_\gamma = 4\,\mathrm{MeV}$. In addition, in order to fit properly, the lower energy resonance must be included for the γ-ray strength function of ^{107}Pd. The pygmy resonance parameters are also less similar to those of tin.

If the speculation that the γ-ray strength functions are supposed to have approximately the same magnitude is true, the ^{108}Pd data are more likely to be normalized to the ^{107}Pd data. This is because all the model parameters are consistent in this case, and there are no fundamental differences in the characteristics of the γ-ray strength functions. In addition, it fits Utsunomiya data very well.

k	C_{pyg} [MeV^{-2}]	σ_{pyg} [MeV]	E_{pyg} [MeV]
0.8	$3.5 \cdot 10^{-7}$	1.6	9.1
k	C_{pyg2} [MeV^{-2}]	σ_{pyg2} [MeV]	E_{pyg2} [MeV]
0.8	$5.0 \cdot 10^{-9}$	1.8	2.3

Table 4.13: Speculative ^{107}Pd resonance parameters.

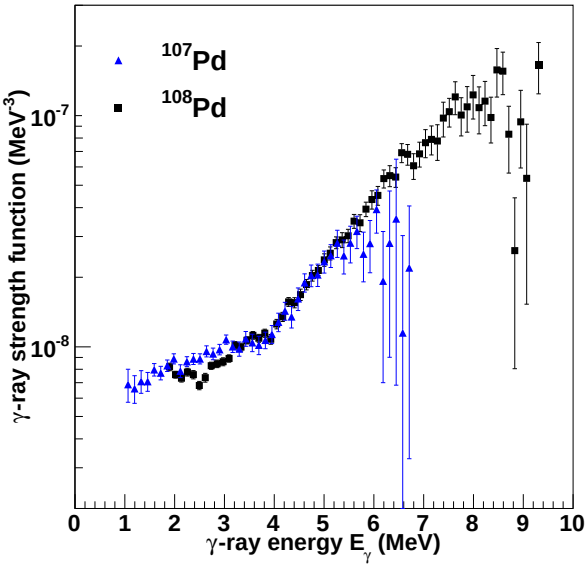

a) Experimental data of ^{108}Pd *normalized to the corresponding magnitude for* ^{107}Pd.

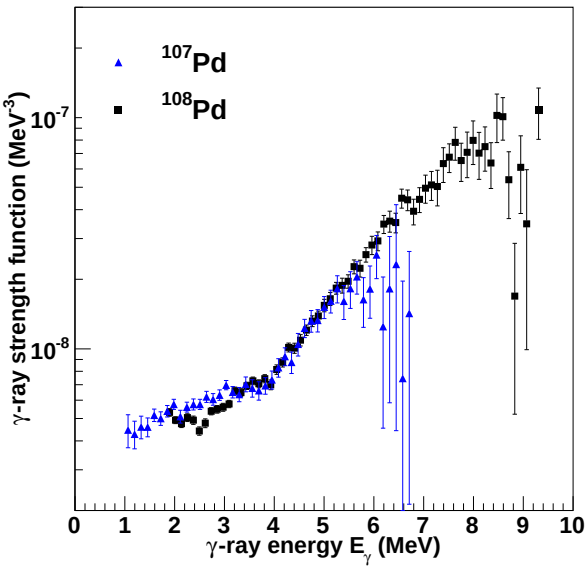

b) Experimental data of ^{107}Pd *normalized to the corresponding magnitude for* ^{108}Pd.

Figure 4.17: The strength functions normalized to eachother. The error bars have been scaled by the normalization constant according to their respective data points.

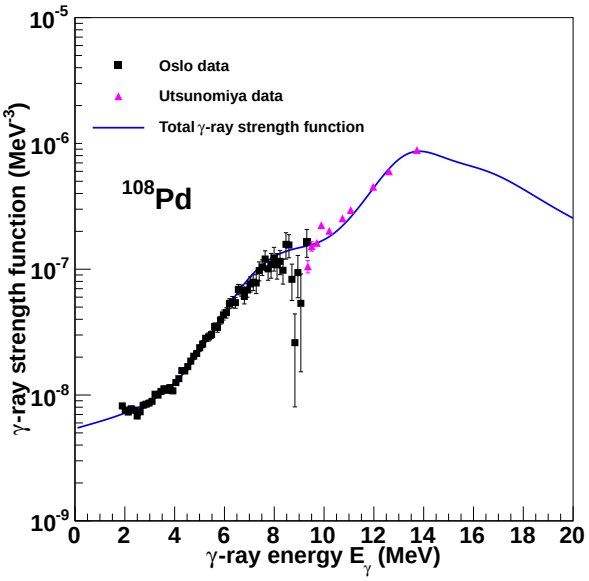

a) Re-normalized γ-ray strength function of ^{108}Pd *compared to models.*

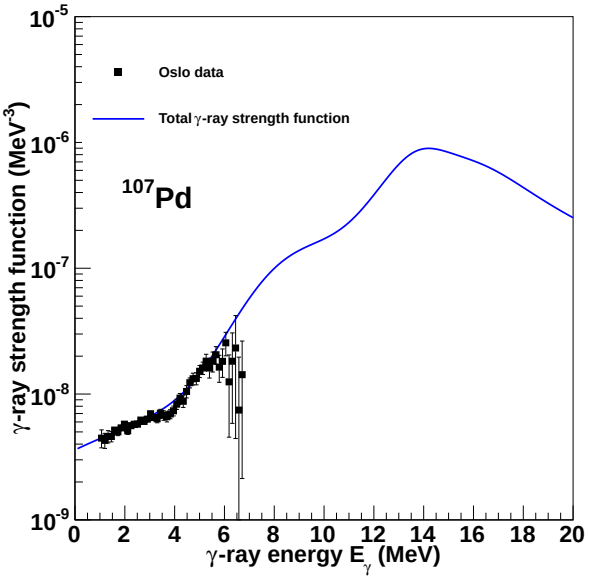

b) Re-normalized γ-ray strength function of ^{107}Pd *compared to models.*

Figure 4.18: The re-normalized γ-ray strength functions compared to models.

Chapter 5

Summary and conclusion

Investigation of the properties in the quasi-continuum of the nuclei ^{107,108}Pd has been performed. In order to obtain experimental data, a ^{108}Pd target was bombarded by 38 MeV ^{3}He ions, and the residuals were then populated by the reactions (^{3}He,α) and (^{3}He,^{3}He'), respectively. The measurements of excitation energy and corresponding γ-ray emissions for the two nuclei were used for extraction of the level densities and γ-ray strength functions according to the Oslo method.

The extracted level densities seem to correspond very well to known characteristics of the nuclei they represent, and nothing ground-breaking was observed. However, the level densities are important in the description of the properties in the quasi-continuum, as well as in the normalization of the γ-ray strength functions.

Comparison of the γ-ray strength functions of ^{107,108}Pd can be divided into two regions of γ-ray energy, i.e. one where they exhibit similar characteristics, and one where they do not. These regions are separated at $E_\gamma \approx 4$ MeV. The extracted γ-ray strength functions were compared to systematic GDR[1] models, and for $E_\gamma > 4$ MeV they both seem to exhibit enhancement as compared to the systematic models. These are most likely caused by resonances related to skin oscillations as observed for tin [5], but other explanations should not be omitted. For ^{108}Pd this observation is further supported by the Utsunomiya data [32, 33].

At lower energy, i.e $E_\gamma < 4$ MeV, the γ-ray strength functions differ in such a way that a conclusion is difficult to make, at least a common conclusion for both nuclei. Unfortunately, the $E_{\gamma,\mathrm{min}}$ limit of ^{108}Pd imposes further difficulties to the investigation in this region. Because of the relatively large discrepancy, the different observations for the two nuclei will be stated separately.

A possible enhancement is observed for ^{107}Pd, between $E_{\gamma,\mathrm{min}}$ and $E_\gamma \approx 4$ MeV. In speculations, this feature has been reproduced by two model approaches. First, by adjusting the temperature in the model calculation, and secondly by including

[1] Giant dipole resonance

a pygmy resonance at $E_\gamma < 4\,\mathrm{MeV}$. The experimental data is fairly reproduced in both cases, and at least, this character does not seem to be caused by an upbend at low E_γ.

For ^{108}Pd on the other hand, this enhancement is completely absent. Very weak signs of an upbend is observed, but this is only for a few data points and is contradicted by data for ^{107}Pd. By considering of these arguments, the upbend at lower energies for ^{108}Pd is not very likely to be present.

The possibility that the normalization of the γ-ray transmission coefficients for the two nuclei are in reality supposed to yield approximately equal magnitudes, is also investigated. A normalization factor of this purpose was deduced, and the experimental γ-ray transmission coefficients of the two nuclei were normalized to eachother, providing γ-ray strength functions of very similar characteristics. If this speculation is true, the experimental γ-ray strength function of ^{108}Pd should be normalized to the magnitude of the corresponding ^{107}Pd data, because all the parameters and characteristics described by the models seem more consistent in that case. The γ-ray strength functions are then both described by the approach of adjusted temperature, by slightly higher values than given by the constant temperature fits, and pygmy resonances with approximately the same parameters as found for tin [5]. The adjusted values of the temperatures correspond very well to the values estimated from the slopes of the level densities. In fact they are also supported by values in [19]. Even if this seems to be a reasonable explanation for the discrepancy between the γ-ray strength functions of the two nuclei, it is still merely a speculation and must not be viewed as a conclusion.

Putting the values of the parameters aside, the bottom line is that the investigation performed in this work strongly supports the presence of pygmy resonances as observed for tin, and contradicts the presence of lower energy enhancement as observed for iron and molybdenum. Regarding the search of a transition between these characteristics in the γ-ray strength functions, this transition seems to occur for elements of lower mass and proton number, since the palladium isotopes investigated in this work exhibit only the characteristics of pygmy resonances.

Because of the large difference in the γ-ray strength functions at lower energies, as well as the relatively high $E_{\gamma,\mathrm{min}}$ for ^{108}Pd, further investigation of palladium isotopes in this mass region is suggested. This is both to determine if the discrepancy in the γ-ray strength functions at low E_γ is true or not, and in light of that determine more specific values for the pygmy resonance parameters. Suggested candidates to be considered are ^{105,106}Pd, where a target of ^{106}Pd can be populated by the same reactions as used in this work. Investigation of nearby elements in this mass region should also be performed, and the neighbouring ^{107}Ag and ^{109}Ag seem to be excellent candidates for this. Elements of lower proton number in this mass region might also be considered, i.e. rhodium and ruthenium, but it

should be noted that these elements are more rare and expensive.

As a last remark, it can be mentioned that a parallel investigation on cadmium isotopes has been performed by Inger-Eli Ruud, which will be interesting to compare to the results of this work since cadmium is close to the mass region investigated.

References

[1] E. Tavukcu, Ph.D. thesis, North Carolina State University, 2002.

[2] A. Voinov, E. Algin, U. Agvaanluvsan, T. Belgya, R. Chankova, M. Guttormsen, G. E. Mitchell, J. Rekstad, A. Schiller and S. Siem. Phys. Rev. Lett. **93**, 142504 (2004).

[3] M. Guttormsen, R. Chankova, U. Agvaanluvsan, E. Algin, L. A. Bernstein, F. Ingebretsen, T. Lönnroth, S. Messelt, G. E. Mitchell, J. Rekstad, A. Schiller, S. Siem, A. C. Sunde, A. Voinov, and S. Ødegård. Phys. Rev. **C 71**, 044307 (2005).

[4] M. Wiedeking, L. A. Bernstein, M. Krtička, D. L. Bleuel, J. M. Allmond, M. S. Basunia, J. T. Burke, P. Fallon, R. B. Firestone, B. L. Goldblum, R. Hatarik, P. T. Lake, I-Y. Lee, S. R. Lesher, S. Paschalis, M. Petri, L. Phair, and N. D. Scielzo. Phys. Rev. Lett. **108**, 162503 (2012).

[5] H. K. Toft, A. C. Larsen, U. Agvaanluvsan, A. Bürger, M. Guttormsen, G. E. Mitchell, H. T. Nyhus, A. Schiller, S. Siem, N. U. H. Syed, and A. Voinov. Phys. Rev. **C 81**, 064311 (2010).

[6] H. K. Toft, A. C. Larsen, A. Bürger, M. Guttormsen, A. Görgen, H. T. Nyhus, T. Renstrøm,1 S. Siem, G. M. Tveten, and A. Voinov. Phys. Rev. **C 83**, 044320 (2011).

[7] M.Guttormsen, A.Bürger, T.E. Hansen, N. Lietaer, Nucl. Instr. and Meth. Phys. Res. **A 648** (2011) 168.

[8] `http://www.mn.uio.no/fysikk/english/research/about/infrastructure/OCL/`

[9] W. R. Leo, Techniques for Nuclear and Particle Physics Experiments, A How-to Approach, Second Revised Edition, Springer-Verlag.

[10] `http://tid.uio.no/~abuerger/jkinz/jkinz.jnlp`

[11] Table of Isotopes, CD ROM Edition, Version 1.0, March 1996, by Richard B. Firestone.

[12] M. Guttormsen, T.S. Tveter, L. Bergholt, F. Ingebretsen and J. Rekstad. Nucl. Instr. and Meth. **A 374** (1996) 371-376.

[13] Cs. Sükösd, B. Galster, I. Licot and M.P. Simonart. Nucl. Instr. and Meth. **A 355** (1995) 552.

[14] M. Guttormsen, T. Ramsøy, and J. Rekstad. Nucl. Instr. and Meth. **A 255** (1987) 518-523.

[15] A. C. Larsen, M. Guttormsen, M. Krtička, E. Běták, A. Bürger, A. Görgen, H. T. Nyhus, J. Rekstad, A. Schiller, S. Siem, H. K. Toft, G. M. Tveten, A. V. Voinov, and K. Wikan. Phys. Rev. **C 83**, 034315 (2011).

[16] T. S. Tveter, L. Bergholt, M. Guttormsen, and J. Rekstad. Nucl. Phys. **A 581** (1995) 220-246.

[17] D. M. Brink, Ph. D. thesis, Oxford University, (1955).

[18] A. Schiller, L. Bergholt, M. Guttormsen, E. Melby, J. Rekstad, and S. Siem. Nucl. Instr. and Meth. **A 447** (2000) 498-511.

[19] T. Egidy and D. Bucurescu. Phys. Rev. **C 72**, 044311 (2005).

[20] T. Egidy and D. Bucurescu. Phys Rev. **C 73**, 049901(E) (2006).

[21] J. Kopecky and M. Uhl. Phys. Rev. **C 41**, 1941 (1990).

[22] A. Gilbert and A. G. W. Cameron. Can. J Phys. **43**, 1446 (1965).

[23] T. Belgya et al. *Handbook for Calculations of Nuclear Reaction Data*, RIPL-2. IAEA-TECDOC-1506 (IAEA, Vienna, 2006).

[24] M. Guttormsen. MAtrix MAnipulation, Oslo Cyclotron Laboratory, November 2002.

[25] M. Guttormsen. ROBIN 1.4, Oslo Cyclotron Laboratory, last modified 20/11 - 2008.

[26] M. Guttormsen. D2RHO 1.1, Oslo Cyclotron Laboratory, last modified 17/3 - 2007.

[27] A. Schiller, L. Bergholt, M. Guttormsen and A. Voinov. RHOSIGCHI 1.3, Oslo Cyclotron Laboratory, last modified 01/05 - 2003.

[28] M. Guttormsen. COUNTING 1.4.2, Oslo Cyclotron Laboratory, last modified 08/01 - 2010.

[29] M. Guttormsen. NORMALIZATION 1.4, Oslo Cyclotron Laboratory, last modified 10/10 - 2008.

[30] `http://www-nds.iaea.org/RIPL-2/`

[31] `http://www-nds.iaea.org/RIPL-3/`

[32] H. Utsunomiya, S. Goriely, H. Akimune, H. Harada, F. Kitatani, S. Goko, H. Toyokawa, K. Yamada, T. Kondo, O. Itoh, M. Kamata, T. Yamagata, Y.-W. Lui, I. Daoutidis, D. P. Arteaga, S. Hilaire, and A. J. Koning. Phys. Rev. **C 82**, 064610 (2010).

[33] `http://www-nds.iaea.org/exfor`